

Contents lists available at ScienceDirect

# Geochimica et Cosmochimica Acta

journal homepage: www.elsevier.com/locate/gca





# A carbon, nitrogen, and multi-isotope study of basalt glasses near 14°N on the Mid-Atlantic Ridge. Part A: Degassing processes

D.V. Bekaert <sup>a,b,\*</sup>, P.H. Barry <sup>a</sup>, J. Curtice <sup>a</sup>, J. Blusztajn <sup>c</sup>, M. Hudak <sup>a</sup>, A. Seltzer <sup>a</sup>, M.W. Broadley <sup>a</sup>, J.A. Krantz <sup>a</sup>, V.D. Wanless <sup>d</sup>, S.A. Soule <sup>e</sup>, E. Mittelstaedt <sup>f</sup>, M.D. Kurz <sup>a</sup>

- <sup>a</sup> Marine Chemistry and Geochemistry Department, WHOI, Woods Hole, MA, USA
- <sup>b</sup> Centre de Recherches Pétrographiques et Géochimiques, Vandoeuvre-lès-Nancy, France
- Geology and Geophysics Department, WHOI, Woods Hole, MA, USA
- <sup>d</sup> Department of Geosciences, Boise State University, 83725 Boise, ID, USA
- <sup>e</sup> Marine Geology and Geophysics Department, The University of Rhode Island, MA, USA
- f Department of Earth and Spatial Sciences, University of Idaho, 83844 Moscow, ID, USA

### ARTICLE INFO

Associate editor: Manuel Moreira

### ABSTRACT

14°N on the Mid-Atlantic ridge (MAR) is one of only a few locations worldwide where volatile-saturated, geochemically enriched mid-ocean ridge basalts (E-MORBs) have been recovered. These basaltic glasses are so gas-rich that CO2-filled bubbles may "pop" when brought to the surface, due to the pressure and temperature change. Although these "popping rocks" have long been regarded as representative samples of un-degassed magmas sourced from the upper mantle, uncertainties regarding both their generation mechanism(s) and the potential effects of gas loss/accumulation processes have hampered unambiguous quantification of the upper mantle volatile element (water, carbon, nitrogen, noble gas) inventory. Fortunately, the extent and consequences of gas loss/accumulation processes can be tested by studying characteristic changes in volatile elements compositions, including  ${}^4\text{He}/{}^{40}\text{Ar}^*$  (where  ${}^{40}\text{Ar}^*$  is  ${}^{40}\text{Ar}$  corrected for atmospheric contamination). To document the mechanism of popping rock generation and potential effects of degassing and gas accumulation processes on MORB volatile systematics, we present a comprehensive volatile characterization (carbon, nitrogen and noble gas systematics) of popping rocks and associated MORBs (n = 19) recently sampled at 14°N on the MAR, including 2 normal MORBs (N-MORB) from an oceanic core complex (OCC) and 17 E-MORBs. In line with previous studies, we find that PR exhibit the lowest  $^4\text{He}/^{40}\text{Ar}^*$  (1.08  $\pm$  0.04) among all MORB samples, lower than the conventional mantle production ratio of 3  $\pm$  1. Such low  ${}^4\text{He}/{}^{40}\text{Ar}^*$  could either (i) derive from accumulation of first-generated bubbles originating from open-system degassing of underlying magmas, or (ii) represent the actual upper mantle production ratio. We summarize the arguments in favor of each of these two scenarios (including the required accumulation times for radiogenic noble gases accumulation, the K/U and <sup>232</sup>Th/<sup>238</sup>U of the upper mantle, popping rock vesicle size distributions, and physical considerations for vesicle growth and upwelling through a basaltic magma), and discuss their implications for the volatile composition of un-degassed magmas from the upper mantle. We find homogenous N isotope compositions (average  $\delta^{15}$ N of  $-4.49 \pm 1.40$  % at 14°N) but variable  $\delta^{13}$ C (from -11 % to -3.4 %), potentially compatible with the expectations for residual dissolved gas after Rayleigh fractionation. However, explaining the light  $\delta^{13}$ C signatures of PR via this process appears incompatible with any of the two scenarios proposed for explaining their low <sup>4</sup>He/<sup>40</sup>Ar\*, which would predict (i) <sup>13</sup>C-enrichements and (ii) no fractionation relative to an initial composition at  $\delta^{13}$ C  $\sim$  -5 ‰, respectively. After correction for solubility-controlled degassing fractionation and potential gas accumulation processes using  ${}^{4}\text{He}/{}^{40}\text{Ar}^{*}$  systematics, we find relatively homogeneous C/ ${}^{3}\text{He}$  ((2.65  $\pm$  0.51)  $\times$  $10^9$ ) but variable C/N (from 125 up to 4578), whose potential origins are discussed as part of a companion paper (Part B: Source effects).

E-mail address: david.bekaert@univ-lorraine.fr (D.V. Bekaert).

 $<sup>^{\</sup>star}$  Corresponding author.

### 1. Introduction

Volatile element systematics (e.g., C, N, noble gas isotopic and elemental ratios) in basaltic glass have the potential to trace mantle source heterogeneities (e.g., Parai et al., 2019; Javoy et al., 1986; Labidi et al., 2020, Marty et al., 2020) provide clues to the origin of enriched geochemical signatures in the MORB mantle (e.g., Marty and Zimmermann, 1999), and are fundamental to understanding the origin of the hydrosphere. However, volatile element variations in MORBs may also arise from secondary processes (e.g., gas loss/accumulation processes) taking place in the oceanic crust. The volatile character of these elements makes them prone to fractionation during open system and/or solubility-controlled degassing of the magmas (Cartigny et al., 2001; Barry et al., 2014; Le Voyer et al., 2015). Gas bubbles produced during magma degassing are largely dominated by CO<sub>2</sub>, the least soluble of the major volatile elements (e.g., Bottinga and Javoy, 1989). As they rise through the magma column, CO2-rich bubbles strip other volatile elements from the basaltic melt (thereby inducing a solubility-controlled fractionation), which progressively depletes the magmas in mantlederived volatiles and makes them sensitive to assimilation of surfacederived volatiles during their emplacement at the sea floor and/or episodes of hydrothermal assimilation in the magma chamber (e.g., Marty et al., 2001; Burnard et al., 2003; Stroncik and Niedermann, 2016). The combined effects of these processes make it difficult to estimate the preeruptive magmatic volatile compositions of MORBs.

The geochemically-enriched section of the slow-spreading Mid-Atlantic Ridge (MAR) between 14° and 15° N (Bougault et al., 1988; Dosso et al., 1991) has long been recognized as one of the most intriguing locations where E-MORBs are observed with no obvious connection to a proximal mantle plume. This location is also the site where one the most gas-rich submarine samples was recovered in dredge 2πD43 of the Soviet oceanographic ship Akademic B. Petrov in 1985, at depths of 3900 m below the surface (Bougault et al., 1988; Sarda et al., 1988; Staudacher et al., 1989; Sarda and Graham, 1990; Javoy and Pineau, 1991; Moreira et al., 1998). The outer glassy portions of the seafloor lavas were so gas-rich that the carbon dioxide filled bubbles (up to 20 vol% vesicularity; Jones et al., 2019) "popped" when brought to the surface, due to the pressure and temperature change, leading to the term "popping rock". Noble gas elemental abundances of the historical "popping rock" 2πD43 were shown to be consistent with minimal gas loss or fractionation during transport from mantle to surface (e.g., Staudacher et al., 1989; Sarda and Graham, 1990; Graham and Sarda, 1991). As a consequence, popping rocks have been considered as representative of mantle source volatile compositions (Javoy and Pineau, 1991). Their analysis notably enabled estimating the upper mantle's carbon content, with fundamental implications for our understanding of the deep carbon cycle (e.g., Pineau et al., 1976; Bottinga and Javoy, 1989; Cartigny et al., 2008; Le Voyer et al., 2017; Jones et al., 2019). One of the most widely used geochemical indicators of gas loss during magma ascent is <sup>4</sup>He/<sup>40</sup>Ar\* (where <sup>40</sup>Ar\* corresponds to the <sup>40</sup>Ar concentration corrected for atmospheric contamination, i.e.,  $^{40}\text{Ar}^{\star} =$  $^{36}$ Ar<sub>sample</sub> ( $^{40}$ Ar/ $^{36}$ Ar<sub>sample</sub> –  $^{40}$ Ar/ $^{36}$ Ar<sub>air</sub>); Sarda and Moreira, 2002; Moreira et al., 1998; Staudacher et al., 1989). Due to the 10-fold lower solubility of Ar in basaltic melts relative to He (Jambon et al., 1986), bubbles are enriched in Ar relative to He, such that any episode of gas loss would tend to increase the <sup>4</sup>He/<sup>40</sup>Ar\* of the residual dissolved gas. Thus, the <sup>4</sup>He/<sup>40</sup>Ar\* of any given MORB sample can be compared with the estimated mantle production ratio (typically, 3  $\pm$  1; Jambon et al., 1986; Staudacher et al., 1989; Marty and Zimmermann, 1999) to assess whether the sample has undergone significant solubility-controlled gas fractionation. To date, popping rock samples have been shown to record the lowest <sup>4</sup>He/<sup>40</sup>Ar\* amongst MORBs worldwide, suggestive of minimal (if any) gas loss. Some other authors have also raised the possibility that the <sup>4</sup>He/<sup>40</sup>Ar\* of most popping rocks are lower than the range of possible mantle production ratio values (Jones et al., 2019). This would potentially indicate a contribution from gas accumulation processes,

implying that the volatile element content of popping rocks may not directly represent the volatile element budget of the mantle source.

The observation of incompatible trace element enrichments of up to a factor of 40 around 14°-15°N on the MAR relative to the depleted basalts found to the north and the south of this region (e.g., Hémond et al., 2006) begs the crucial question of, which geological reservoir does the mantle source of popping rocks represent? Several models have attempted to explain the geochemical enrichment at  $\sim 14^{\circ}$  N, including (i) melting of old subducted crust or sediments (Staudacher et al., 1989); (ii) relics of sub-continental lithospheric mantle removed from the continents during continental break up (Bonatti et al., 1992; Dosso et al., 1999; Hoernle et al., 2011); (iii) recycled alkali basaltic seamounts (Hémond et al., 2006; Ulrich et al., 2012); (iv) existence of a ridgecentered mantle plume (e.g., Dosso et al., 1991). The latter scenario could be related to a developing triple junction at this location (Bougault et al., 1988), or arise from the deflection of upwelling Researcher Ridge plume material towards the west-ward migrating MAR (Long et al., 2019). Most of these models have used radiogenic isotope (e.g., Pb, Sr, Nd) systematics, major element (e.g., K2O/ TiO2), and trace element ratios (e.g., La/Sm), to discriminate between the so-called normal (N)-MORB and E-MORB end-members for global MORBs (Hofmann, 2007). To what degree these mantle geochemical heterogeneities contribute to volatile element variations along the MAR remains unknown. Yet, answering this question could have far reaching implications for the surmised representativeness of popping rocks for the volatile content of the whole upper mantle.

The potential value of combining radiogenic and volatile element isotope systematics to distinguish mantle source heterogeneities from the effect of secondary processes (including bubble accumulation) remains poorly explored. In an attempt to fill this gap, we present new isotopic data for volatile (carbon, nitrogen, noble gases) and radiogenic (Pb, Sr, Nd) elements, as well as the abundances of major and trace elements, of popping rocks and associated MORBs (n = 19) collected between 2016 and 2018 near 14°N on the MAR (Péron et al., 2019; Jones et al., 2019; Parnell-Turner et al., 2018; Table 1, Fig. 1). Major, trace, and volatile (4He/40Ar\*, carbon, nitrogen) element data are presented and discussed here (Part A), with the overarching goal of better constraining the effects of secondary processes (vesiculation, gas loss/ accumulation) on volatile element systematics in MORBs. Most of the discussion aims at better constraining the series of processes contributing to the formation of popping rocks, as well as the possibility to use the <sup>4</sup>He/<sup>40</sup>Ar\* to correct measured volatile compositions for the effects of these secondary processes. Radiogenic isotope and additional noble gas (He and Ne isotope) data are presented and discussed with volatile element systematics as part of a companion manuscript (Part B), with the objective of specifically discussing the extent and origin of upper mantle geochemical heterogeneities near 14°N on the MAR.

# 2. Methods

# 2.1. Overview

All samples analyzed in this study were collected between 2016 and 2018 near 14°N on the MAR using R/V Atlantis and the human occupied submarine vehicle Alvin (Péron et al., 2019; Jones et al., 2019; Parnell-Turner et al., 2018; Table 1; Fig. 1). The sample set consists of 5 popping rocks (hereafter "PR"), 6 low-vesicularity (<3 vol%) MORBs with PR-like trace element patterns ("PRTE-LV"), 6 non-popping rocks ("NPR"), and 2 MORBs recovered from oceanic core complexes ("OCC"), off-axis from the MAR (Parnell-Turner et al., 2018) (Fig. 1). Because measurements presented in this study are destructive, the analysis of (i) major and trace elements, (ii) noble gases by step-crushing, (iii) carbon and nitrogen by bulk crushing, (iv) radiogenic isotopes, were performed on separate aliquots of each sample. Given that basaltic glass is relatively homogeneous, it is assumed that measurements on separate aliquots are directly comparable. Sample extraction, purification, and

Table 1
Sampling details (latitude, longitude, depth). The classification refers to popping rocks ("PR"), non-popping rocks ("NPR"), MORBs recovered from oceanic core complexes ("OCC"), and low-vesicularity (<3 vol%) MORBs with popping rock-like trace element patterns ("PRTE-LV"). NPR\*: NPR sample dredged at the same latitude as OCCs. See also Jones et al., (2019).

Sample	Classification	Latitude (deg)	Longitude (deg)	Depth (m)
AL4818-	PR	13.7737	-45.0108	3672
003				
AL4821-	PR	13.7736	-45.0104	3666
055				
AL4821-	PR	13.7738	-45.0091	3684
058				
AL4821-	PR	13.7710	-45.0090	3706
059				
AL4820-	PR	13.7675	-45.0081	3773
037				
AL4818-	NPR	13.7749	-45.0132	3697
006				
AL4819-	NPR	13.7755	-45.0499	3566
029				
AL4820-	NPR	13.7670	-45.0135	3852
032				
AL4820-	NPR	13.7688	-44.9982	3492
045				
AL4824-	NPR	14.0888	-45.0201	2877
104				
AL4959-	NPR*	13.8116	-45.0146	3522
406				
AL4822-	OCC	13.8182	-44.9514	2767
064				
AL4822-	OCC	13.8179	-44.9513	2749
065				
AL4818-	PRTE-LV	13.7741	-45.0067	3773
001		40 40		
AL4818-	PRTE-LV	13.7743	-45.0074	3761
002	DD#E 111	10.7600	45.00.41	0655
AL4820-	PRTE-LV	13.7692	-45.0041	3657
040	DDEE 111	10.7605	45.0006	0645
AL4820-	PRTE-LV	13.7695	-45.0026	3645
041		10.505	45.0006	0645
- AT 4000	- DDTE IV	13.7695	-45.0026	3645
AL4820-	PRTE-LV	13.7698	-45.0008	3619
043	DDTE IV	12.7706	45.0100	2021
AL4821-	PRTE-LV	13.7796	-45.0120	3821
049				

analytical procedures are described below for each series of analyses. This manuscript (Part A) focuses on volatile element systematics (noble gases, C, N), while the companion manuscript (Part B) presents and discusses major and trace element, as well as radiogenic isotope data.

# 2.2. Major and trace element analyses

Major and trace element concentrations were measured using the Cameca SXFive electron microprobe and the Thermo-Electron X-Series II Quadrupole Inductively Coupled Plasma Mass Spectrometer, respectively, at Boise State University. Sample preparation techniques and analyses for major and trace elements are described in detail in Schwartz et al. (2018) and Jones et al. (2019).

# 2.3. Noble gas step-crushing analyses

Step-crushing analyses were conducted at Woods Hole Oceanographic Institution (WHOI) on clean, centimeter-sized, glass fragments, typically weighing 1-2 g. Helium and neon isotopes were analyzed using a MAP 215-50 mass spectrometer in the WHOI Isotope Geochemistry Facility (IGF), as described by Kurz et al. (2005), Kurz et al. (2009), and Péron et al. (2019). Argon isotopes were measured using a dedicated Quadrupole Mass Spectrometer (Hiden), attached to the same extraction line. Helium, neon, and argon were separated using two automated cryogenic traps, one nude stainless steel for heavy noble gases and one charcoal for helium. All measurements were made by crushing in vacuum, using well-established magnet-activated low-blank procedures with a magnetic stainless steel ball (e.g., Kurz et al., 2005; Kurz et al., 2009). The quantities of gas introduced into the extraction line and mass spectrometers were controlled by capacitance manometry, followed by a pre-measurement with a quadrupole mass spectrometer, and volumetric splitting as necessary to match sample size with standard size. Pregettering capacitance manometry measurements were used to calculate  $CO_2/^3$ He ratios (hereafter noted  $C/^3$ He, Table 2–5), assuming that CO<sub>2</sub> constitutes most of the volatiles released by crushing (Moore et al., 1977). As stated in Péron et al. (2019), noble gas concentrations are so elevated in these samples that they could be measured many times by repeated crushing. Noble gas analyses of PR samples AL4818-003, AL4821-055, AL4821-058, and PRTE-LV AL4820-041 were previously reported by Péron et al. (2019). While He abundance, C/3He, and Ar isotope data are presented as part of this manuscript (Part A; Table 2-5),

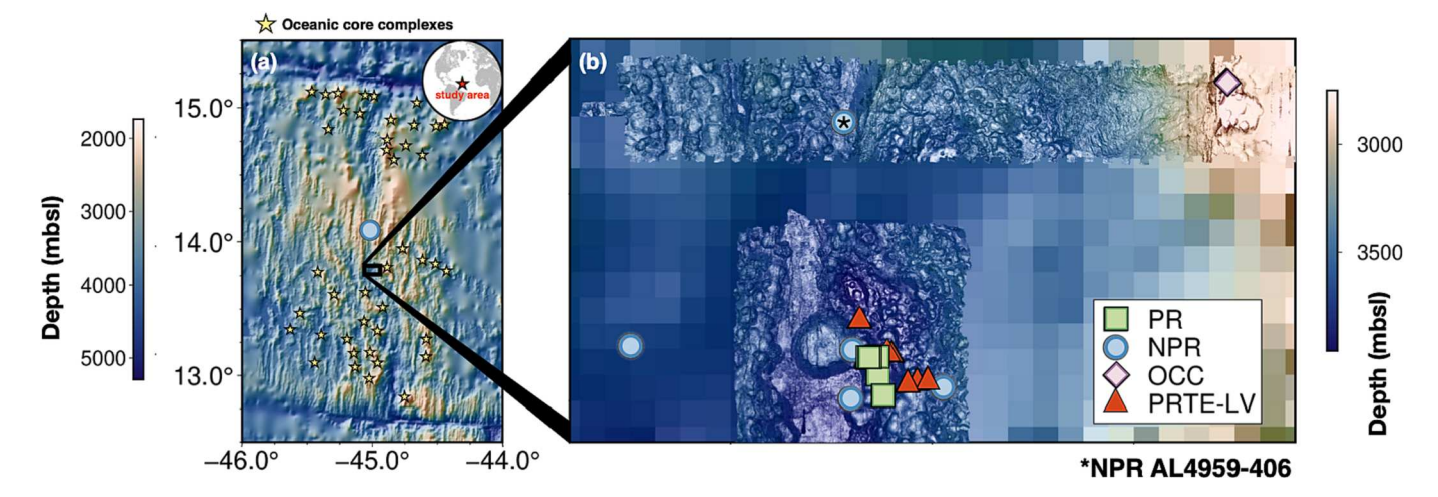


Fig. 1. High-resolution bathymetric maps obtained via the autonomous underwater vehicle (AUV) Sentry, showing the location of the samples from cruise AT33-03 of R/V Atlantis on the MAR analyzed in this contribution. (a) Location of the study area, at the junction between the 14°N magmatic segment and the 13°N tectonic segment. Black rectangle shows the contours of panel (b). The locations of oceanic core complexes (yellow stars) and NPR sample AL4824-104 are also reported. (b) 1 m resolution bathymetric map showing the spatial distribution of MORB samples analyzed in this study. Depth given in meters below sea level (mbsl). Distribution of oceanic core complexes is . (For interpretation of the references to colour in this figure legend, the reader is referred to the web version of this article.) reproduced from Smith et al., (2006)

**Table 2** Step crushing He and Ar analyses of PR samples analyzed in this study, and determination of  $C/^3$ He and  $^4$ He/ $^{40}$ Ar\*.

ample	Туре	weight	crushing step	<sup>4</sup> He (x10 <sup>-6</sup> cm <sup>3</sup> STP/g)	C/ <sup>3</sup> He (x10 <sup>09</sup> )	$^{36}$ Ar (x10 <sup>-10</sup> cm <sup>3</sup> STP /g)	$^{40}$ Ar/ $^{36}$ Ar	1σ	<sup>4</sup> He/ <sup>40</sup> /
L4818-003	PR	1.4	1	0.43	3.30	0.31	14,318	558	1.0
			2	0.92	3.13	0.59	15,522	963	1.0
			3	1.16	3.28	0.73	15,593	427	1.0
			4	5.58	3.10	6.23	7905	891	1.2
			5	4.66	3.28	4.77	8604	1064	1.2
			7	0.74	3.02	0.48	15,216	1124	1.0
			8	0.41	2.25	0.34	12,364	518	1.0
			9	1.24	3.11	0.78	15,239	498	1.1
			10	8.04	3.62	5.37	12,665	531	1.2
			11	1.51	3.10	3.82	4005	46	1.1
			12	2.01	3.37	1.31	15,053	347	1.0
							15,799		
			13	3.28	3.19	1.98		359	1.1
			14	0.39	3.14	0.31	12,732	683	1.0
			15	4.04	3.18	2.23	16,071	505	1.1
			16	2.9	10.5	7.14	4234	129	1.0
			17	4.28	3.09	2.48	14,984	449	1.2
			18	0.92	3.16	0.60	15,233	852	1.0
			19	0.74	2.99	0.47	15,199	2255	1.1
			20	1.49	2.91	1.56	9062	177	1.1
			21	1.35	3.11	0.94	14,083	298	1.0
			22	0.76	3.21	0.49	16,229	649	1.0
			23	2.77	3.12	1.77	15,612	2841	1.0
			23 24	2.29	3.13	1.61	14,177	271	1.0
					3.13				
			25	1.67		1.16	13,742	304	1.1
			26	2.62	3.15	1.68	14,465	320	1.1
			27	1.80	3.13	1.10	15,556	335	1.1
			28	0.76	2.83	0.51	13,907	3800	1.1
			29	1.64	2.71	0.95	15,336	377	1.1
.4821-055	PR	1.94	1	0.94	3.14	0.61	15,122	322	1.0
14021-033	110	1.54						322	
			2	5.65	2.34	4.52	n.d.		1.1
			3	2.93	3.29	2.24	n.d.		1.0
			4	3.13	7.18	2.85	11,873	599	0.9
			5	0.55	2.72	0.37	14,931	899	1.0
			7	3.61	3.33	2.66			1.0
			8	0.58	2.56	0.39	14,711	4289	1.0
			9	7.16	3.04	5.23	n.d.		1.1
			10	3.67	2.91	3.24	n.d.		1.1
			11	1.2	2.93	0.82	14,120	311	1.1
			12	1.43	2.97	0.92	14,902	283	1.1
			13	1.74	3.04	1.37	12,582	183	1.0
						0.85			
			14	1.31	2.85		14,537	270	1.1
			15	0.62	2.83	0.40	14,869	432	1.1
			16	0.77	3.04	0.50	15,132	354	1.0
			17	0.83	2.86	0.52	15,076	1420	1.1
			18	1.64	2.85	0.99	15,579	329	1.1
			19	0.79	2.92	0.51	14,838	452	1.1
			20	0.94	3.24	0.59	15,611	431	1.0
			21	0.74	2.85	0.48	14,854	418	1.1
			22	0.59	2.97	0.22	14,339	688	1.9
			23	0.85	2.82	0.52	14,937	360	1.1
			23 24	2.34	2.83	1.79	n.d.	300	1.1
								720	
			25	1.40	2.73	0.87	15,588	728	1.0
			26	0.68	2.90	0.43	15,064	392	1.1
			27 28	0.48 0.35	2.72 2.69	0.33 0.23	14,463 14,696	490 985	1.0 1.0
4821-059	PR	1.40346	1 2	6.78	13.8	431	548	6	0.6
				2.31	3.50	1.50	15,131	271	1.0
			3	0.37	3.30	0.28	13,143	718	1.0
			4	0.20	5.73	0.63	3080	91	1.2
			5	1.69	3.03	1.33	12,039	287	1.1
			7	3.74	5.62	43.6	904	5	1.4
			8	0.75	2.60	0.79	8623	187	1.1
				0.38	3.60	0.31	12,644	613	1.0
			9						
					3.29	16.1	3627	179	1.3
			10	6.99	3.29 3.09	16.1 2.77	3627 13.861	179 429	1.3 1.3
			10 11	6.99 4.91	3.09	2.77	13,861	429	1.3
			10 11 12	6.99 4.91 7.99	3.09 4.15	2.77 14.7	13,861 4432	429 78	1.3 1.3
			10 11	6.99 4.91	3.09	2.77	13,861	429	1.3

(continued on next page)

Table 2 (continued)

Sample	Туре	weight	crushing step	<sup>4</sup> He (x10 <sup>-6</sup> cm <sup>3</sup> STP/g)	C/ <sup>3</sup> He (x10 <sup>09</sup> )	<sup>36</sup> Ar (x10 <sup>-10</sup> cm <sup>3</sup> STP /g)	<sup>40</sup> Ar/ <sup>36</sup> Ar	1σ	<sup>4</sup> He/ <sup>40</sup> Ar
			16	2.37	2.87	3.07	6975	91	1.2
			17	1.20	2.67	0.70	13,571	5394	1.3
			18	1.01	2.91	16.9	784	4	1.2
			19	0.25	2.92	0.18	13,530	2445	1.1
			20	1.78	3.02	4.32	4065	37	1.1
			21	1.03	2.85	10.6	1155	7	1.1
			22	0.63	3.01	0.66	8760	306	1.1
			23	0.67	2.54	0.39	14,243	1010	1.2
			24	0.18	2.75	0.15	12,487	1200	1.0
			25	0.20	2.02	0.31	5812	573	1.2
			26	0.082	1.15	0.07	10,116	727	1.2
AT 4020 027	DD.	2 001 01	1	0.02	2.24	1.70	F077	F.7	1.1
AL4820-037	PR	3.09191	1 2	0.93 2.24	3.24 12.1	1.79 9.06	5077 3055	57 60	1.1 0.9
			3	2.76	3.12	9.06	3239	452	1.0
			3 4	7.21	3.12	6.99	9525	639	1.0
			5	0.28	3.15	0.22	13,346	471	1.1
			3 7	5.31	3.53	6.81	7687	663	1.1
			8	5.44	2.82	9.20	5548	361	1.1
			9	1.69	2.97	1.43	10,903	932	1.1
			10	1.61	5.57	3.05	10,903 5500	282	1.1
			10	0.98			8297	110	1.0
			12	1.00	3.73 2.93	1.19 0.60	14,908	503	1.0
			13	1.37	3.03	3.26	3979	227	1.1
			14	1.23	11.3	6.10	2371	25	1.0
			15	0.64	9.42	2.84	2504	26	1.0
			16	0.66	4.03	0.47	13,330	409	1.1
			17	0.89	8.82	5.33	2974	177	0.6
			18	0.65	3.04	0.43	14,296	317	1.1
			19	1.00	2.84	1.34	6901	67	1.1
			20	0.64	2.75	0.41	14,250	333	1.1
			21	0.92	6.81	1.79	5212	69	1.0
			22	0.77	2.97	0.51	13,992	310	1.1
			23	0.70	2.96	0.51	12,844	294	1.1
			24	0.62	3.00	1.66	3808	47	1.1
			25	1.26	3.04	1.24	9317	1219	1.1
			26	0.49	5.13	3.11	1825	14	1.0
			27	0.63	3.62	1.08	5661	72	1.1
			28	0.62	2.87	0.42	13,735	281	1.1
			29	0.58	3.02	0.37	14,889	648	1.1
			30	0.48	4.55	1.98	2593	22	1.1
			31	0.43	2.90	0.30	14,063	359	1.0
			32	0.79	2.85	1.39	5513	81	1.1
			33	0.79	5.39	1.30	5446	73	1.1
			34	0.75	2.69	0.52	12,981	605	1.1

He and Ne isotope data are reported and discussed as part of the companion manuscript (Part B).

# 2.4. Nitrogen and carbon analyses

# 2.4.1. Gas extraction

Nitrogen isotope measurements of clean glass fragments ranging from ~ 60 mg up to over 1 g were performed using a high-precision multi-collector Nu Noblesse mass spectrometer recently set up in the Barry Lab at WHOI. The system is equipped with two stainless steel hydraulic crushers for gas extraction, which are connected to a vacuum gas purification line and a RGA Quadrupole Mass Spectrometer (see sample extraction and purification procedures described by Barry et al. (2012). In this procedure, visually fresh and cleaned oceanic basalt glasses are first loaded into the two crushers, which are baked at 100 °C overnight to remove any adsorbed atmospheric nitrogen. Once crushers have cooled to room temperature, at least one blank measurement was carried out to (i) verify the absence of a leak and (ii) enable subsequent blank correction. If the blank was low (typically  $\leq 1 \times 10^{-6} \text{ cm}^3 \text{STP N}_2$ ), then the first sample was crushed using a hydraulically operated crushing press at 5000 psi, effectively releasing trapped vesicle-sited gas. Released CO2, H2O, and other condensable gases were separated from nitrogen gas on a Pyrex cold finger held at liquid-nitrogen

temperature. After 3 min of trapping, the cold finger was isolated and non-condensable gases remaining in the line were separated into two gas fractions dedicated to (i) N2 abundance determination on a Quad Mass Spectrometer (QMS) and (ii) sample purification for high precision N isotope measurements (Barry et al., 2012; see section 2.4.2), respectively. Condensable gases (mainly CO<sub>2</sub> in the case of popping rocks) were then released from the Pyrex finger at room temperature and transferred for 20 min into a glass ampoule held at liquid-nitrogen temperature. This glass ampoule contains 100 mg of Alpha Aesar Copper Oxide(II) and a few grains of crystalline Alpha Aesar Silver Powder (-10  $\pm$  20 mesh Premion 99.99 %), previously baked at 560 °C for at least one hour. The glass ampoule containing most of the CO<sub>2</sub> released upon crushing was eventually flame-sealed, baked at 560 °C for another hour in order to quantitatively remove H<sub>2</sub>O and sulfur-bearing species, and sent for C isotope determination at the NOSAMS facility (WHOI) (see section 2.5.3).

# 2.4.2. Nitrogen isotope measurements

The gas fraction dedicated to N isotope measurements was exposed to a copper oxide (CuO) finger (at 850  $^{\circ}$ C) in the presence of a platinum foil catalyst (at 1000  $^{\circ}$ C), which promotes oxidation of carbonaceous (CO, C<sub>2</sub>H<sub>4</sub>) and nitrogenous (NO) species to CO<sub>2</sub> and NO<sub>2</sub>, while any residual hydrogen and sulfur were oxidized to H<sub>2</sub>O and SO<sub>2</sub>,

 $\begin{tabular}{ll} \textbf{Table 3} \\ \textbf{Step crushing He and Ar analyses of NPR samples analyzed in this study, and determination of C/$^3$He and $^4$He/$^4$^Ar*.} \end{tabular}$ 

Sample	Туре	weight	crushing step	<sup>4</sup> He (x10 <sup>-7</sup> cm <sup>3</sup> STP/g)	C/ <sup>3</sup> He (x10 <sup>09</sup> )	<sup>36</sup> Ar (x10 <sup>-11</sup> cm <sup>3</sup> STP/g)	$^{40}$ Ar/ $^{36}$ Ar	1σ	<sup>4</sup> He/ <sup>40</sup> Ar
AL4818-006	NPR	2.21	1	1.89	2.66	0.93	2441	49	9.4.0
			2	1.34	2.24	0.15	7754	546	12.3
			3	2.20	2.43	0.26	8258	375	10.4
			4	1.63	2.03	0.17	8026	409	12.2
			5	2.56	1.76	0.37	6267	239	11.5
			6	1.02	0.78	0.18	3625	194	17.0
AL4819-029	NPR	3.21032	1	5.59	1.94	1.71	1337	14	31.3
			2	9.76	1.94	0.27	12,655	405	29.3
			3	9.92	1.89	0.62	5356	108	31.4
			4	13.3	1.84	0.56	8401	1081	29.1
			5	9.99	1.95	0.19	17,290	890	31.6
			6	15.5	2.00	1.21	4624	255	29.4
			7	14.5	1.75	2.61	1915	55	34.4
			8	12.8	1.57	2.05	2086	201	35.0
			9	3.99	1.25	0.32	3433	97	40.3
AL4820-045	NPR	2.45725	1	1.88	1.07	6.00	375	9	39.4
AL4020-043	NFK	2.43/23	2	2.52	1.27	1.54	745	3	36.6
			3	4.32	1.58	0.38	3191	19	39.5
			4	2.86	1.31	0.40	1996	126	41.8
			5	18.3	1.48	1.47	3231	61	42.3
			6	8.17	1.43	6.06	630	45	40.3
			7	2.15	2.81	0.15	3159	5	49.3
			8	5.51	1.11	1.73	974	197	46.9
AT 4004 104	NDD	1 1 400	1	4.00	0.45	0.60	4000	100	10.0
AL4824-104	NPR	1.1409	1 2	4.22 9.87	2.45	0.62	4029	183	18.2 20.0
			3	9.87 12.1	2.47 2.56	0.63 5.96	8081	305 17	19.0
							1362		
			4 5	10.7 9.45	2.65 2.77	2.81 0.61	2302 9100	53 364	18.9 17.5
			6	16.5	2.83	5.22	2133	28	17.3
			7	5.23	2.68	0.47	6610	28 256	17.2 17.6
			8	3.55	1.86	0.71	2881	120	19.4
AL4959-406	NPR*	2.14152	1	2.13	4.55	1.13	17,853	2278	1.10
			2	1.26	3.77	12.9	1176	21	1.10
			3	3.14	3.32	1.54	19,078	1128	1.10
			4	1.71	3.54	1.38	12,069	623	1.10
			5	4.32	3.6	1.70	25,009	1576	1.00
			6	1.04	3.68	0.45	22,316	1991	1.00
			7	4.04	3.42	2.70	14,815	594	1.00
			8	2.68	2.95	0.99	25,065	2766	1.10
			9	1.21	2.48	0.41	26,309	1993	1.10

Table 4 Step crushing He and Ar analyses of OCC samples analyzed in this study, and determination of  $C/^3$ He and  $^4$ He/ $^{40}$ Ar\*.

Sample	Classification	weight	crushing step	<sup>4</sup> He (x10 <sup>-7</sup> cm <sup>3</sup> STP/g)	C/ <sup>3</sup> He (x10 <sup>09</sup> )	<sup>22</sup> Ne (x10 <sup>-12</sup> cm <sup>3</sup> STP/g)	<sup>36</sup> Ar (x10 <sup>-11</sup> cm <sup>3</sup> STP /g)	<sup>40</sup> Ar/ <sup>36</sup> Ar	1σ	<sup>4</sup> He/ <sup>40</sup> Ar*
AL4822-064	OCC	1.19782	1	8.67	2.44	1.48	1.53	20,293	2246	2.8
			2	7.38	2.14	1.20	1.33	17,060	2164	3.3
			3	2.45	2.61	0.47	0.41	22,995	922	2.6
			4	3.18	1.89	0.57	0.46	21,136	2022	3.3
			5	1.33	0.02	22.6	34.9	401	2	3.6
AL4822-065	occ	0.9391	1	6.83	2.47	37.1	0.65	665	8	2.8
			2	4.71	2.02	0.70	0.61	23,427	3793	3.3
			3	12.5	1.99	1.76	1.56	22,591	2332	3.6
			4	5.27	1.61	0.62	0.52	21,772	984	4.7
			5	4.72	0.94	0.53	0.51	18,802	1082	5.0
			6	0.11	n.d.	0.03	0.06	6321	76	3.0

Table 5
Step crushing He and Ar analyses of PRTE-LV samples analyzed in this study, and determination of  $C/^3$ He and  $^4$ He/ $^{40}$ Ar\*.

Sample	Classification	weight	crushing step	<sup>4</sup> He (x10 <sup>-7</sup> cm <sup>3</sup> STP/g)	C/ <sup>3</sup> He (x10 <sup>09</sup> )	<sup>36</sup> Ar (x10 <sup>-11</sup> cm <sup>3</sup> STP /g)	$^{40}$ Ar/ $^{36}$ Ar	1σ	$^{4}$ He/ $^{40}$ Ar*
AL4818-002	PRTE-LV	1.37599	1	3.23	2.44	1.98	7710	993	2.2
			2	6.94	2.00	2.64	12,986	795	2.1
			3	6.32	2.02	2.12	12,795	1552	2.4
			4	5.85	0.95	1.39	10,753	1517	4.0
AL4820-043	PRTE-LV	0.96187	1	4.30	2.93	38.9	1173	20	1.3
			2	8.81	2.53	35.6	1946	33	1.5
			3	1.64	2.37	56.9	488	5	1.5
			4	1.25	2.73	41.8	501	6	1.5
			5	31.5	2.76	29.3	24,164	3856	1.6
			7	32.2	2.88	17.3	23,145	641	1.4
			8	22.6	2.83	12.6	22,592	1740	1.4
			9	32.1	2.96	16.8	24,508	518	1.3
			10	25.6	2.98	243	1645	10	1.3
			11	25.9	2.87	50.1	6882	93	1.3
			12	17.2	2.78	6.15	21,033	788	1.4
			13	22.5	4.16	32.3	5515	91	1.3
			14	16.4	2.91	8.48	14,794	617	1.3
			15	13.3	2.82	4.13	23,401	1291	1.4
			16	11.3	2.27	3.55	21,813	1186	1.5
			17	19.1	2.65	23.6	6315	114	1.3
			18	12.5	2.39	3.48	24,860	1992	1.5
			19	8.73	2.44	2.38	24,230	3132	1.5

respectively. All condensable species produced at this stage are adsorbed onto a Pyrex cold finger held at liquid nitrogen temperature. Oxygen was then reabsorbed back onto the CuO finger at a lower temperature (<600 °C) before the oxidized gas was inlet into the Noblesse mass spectrometer. Due to the highly variable volatile contents of MORBs analyzed, gases were commonly "split down" by performing volume expansions in the vacuum purification line, which was required to avoid saturating the collectors. Appropriate split fractions of purified nitrogen were calculated based on the amount of N2 detected on the QMS for the first gas fraction. During N isotope analysis, we simultaneously measure m/z = 28 and 29. In total, 20 data collection cycles are run per sample. Background levels are monitored between sample measurements to apply a background subtraction to all data. The nitrogen isotope ratio is calculated by extrapolating the data back to time zero (i.e., time of inlet into the mass spectrometer) using a linear fit. A CO correction is made by directly measuring CO at m/z 28 and then applying a correction to the 28 and 29 peaks. This correction assumes that the CO contribution at mass 29 is 1.09 % of the contribution at mass 28, based on the abundance ratio of <sup>13</sup>C to <sup>12</sup>C in air (Graven et al., 2020). Notably, precise characterization of standards, blanks and correction factors are critical when making high precision N-isotope measurements (Supplementary Information). The automatization of standard measurements allows a significant number of N2 standards to be measured (about 50 analyses per day on average), thus enabling precise characterization of the N<sub>2</sub> standard's composition, as well as quantification of (and correction for) linearity effects in the mass spectrometer. A full description of the N2 extraction system and additional information about the analytical performance as well as corrections are provided in the Supplementary Information.

### 2.4.3. Carbon isotope measurements

Glass ampoules containing  $CO_2$  were provided to the National Ocean Sciences Accelerator Mass Spectrometry facility (NOSAMS) for quantification and purification. Each glass ampoule was loaded into a cracking device attached to a 10-port vacuum system. Samples were transferred to a measuring volume in vacuum at liquid nitrogen temperature. The gas also passed through a glass trap containing an isopropanol/dry ice slurry. The samples were then heated and expanded in the calibrated volume region and quantified using an MKS 222BA-100 torr capacitance manometer. Uncertainty on the  $CO_2$  quantification was  $\pm$  0.2  $\mu$ moles.

The cleaned and quantified gas was then transferred to a portable glass ampoule for  $\delta^{13} \text{C}$  measurement.  $\delta^{13} \text{C}$  analyses were performed on a VG PRISM-II stable isotope ratio mass spectrometer (SIRMS) with dual inlet that contained a 20-port gas cracker manifold prep system. Sample gas was compared to a known reference gas that had been calibrated against NBS-19 calcite and corrected to VPDB isotopic standards. Uncertainty for the majority of the  $\delta^{13} \text{C}$  mass spec results is  $\pm$  0.1 per mil.

### 3. Results

# 3.1. Major and trace element systematics

Major and trace element values are reported in *Supplementary Information*. The 19 MORB samples analyzed in this study span a wide range in compositions, from E-MORB (PR-affiliated samples) to N-MORB (OCC samples) end-members (Fig. 2). Non-popping rock samples (NPR) span a wider range of chemical compositions across the T-MORB to E-MORB ranges. Taken together, these data thus support the existence of strikingly large geochemical heterogeneities at the local scale, near 14°N on the MAR (Péron et al., 2019; Bekaert et al., Part B).

# 3.2. ${}^{4}He/{}^{40}Ar^{*}$ systematics

Among all the MORBs analyzed in this study, PR samples exhibit both the highest  $^4\text{He}$  concentrations (up to  $\sim7~x~10^{-5}~\text{cm}^3\text{STP/g}$ ), the highest fractions of total  $^4\text{He}$  released upon crushing ( $\sim98$ %, consistent with their high vesicularities), and the lowest  $^4\text{He}/^{40}\text{Ar}^*$  ratios (average value of PR samples: 1.08  $\pm$  0.04 (10)), consistent with previous studies (Sarda and Moreira, 2002; Moreira et al., 1998; Staudacher et al., 1989; Table 2-5). Individual  $^4\text{He}/^{40}\text{Ar}^*$  data from multiple stepwise crushing steps are shown on Fig. 3.

As observed in previous studies (Jones et al., 2019), the homogeneous  $^4\text{He}/^{40}\text{Ar}^*$  of PR samples (ranging from 1.04 to 1.14; Table 1) is seemingly low compared to the putative mantle production ratio, typically considered to lie within the range  $3\pm1$  (Jambon et al., 1986; Staudacher et al., 1989; Marty and Zimmermann, 1999) – although some authors have proposed slightly different values (e.g., in the range 1.6 to 4.2, (Graham, 2002)) (Fig. 3). Likewise, the  $^4\text{He}/^{^40}\text{Ar}^*$  of PRTE-LV samples (in the range 1.3–2.2; Table 1) plot on the low end of the accepted mantle production range. Other samples exhibit higher

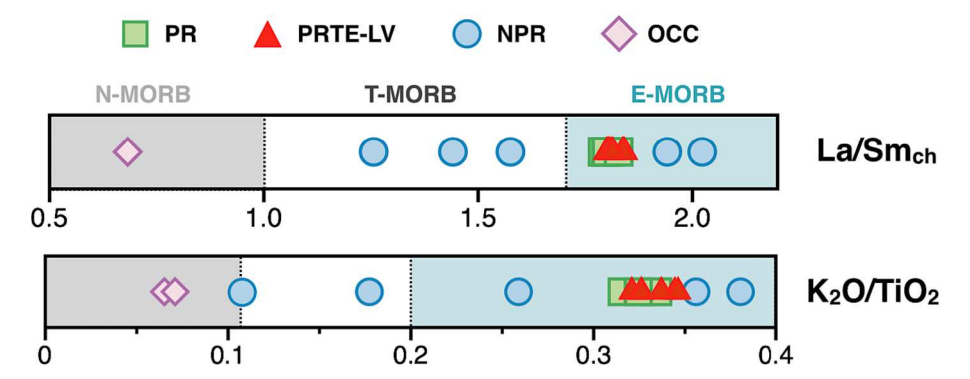


Fig. 2. Major (e.g., K<sub>2</sub>O/TiO<sub>2</sub>) and trace (e.g., La/Sm, normalized to the chondritic ratio; Lodders (2021)) element composition of MORB samples analyzed in this study. Both systems are used to classify PR-affiliated rocks (PR and PRTE-LV) as E-MORBS and OCC samples as N-MORBs. The corresponding data are reported in Supplementary Information.

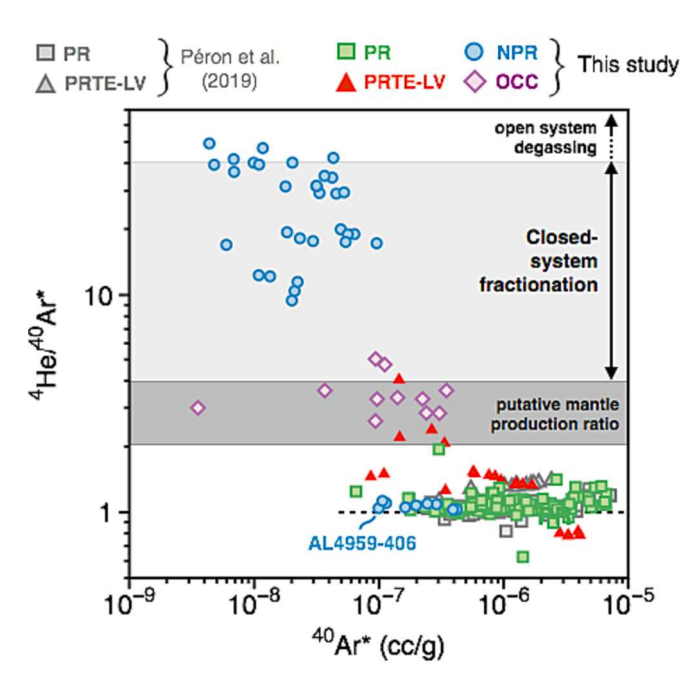


Fig. 3. <sup>4</sup>He/<sup>40</sup>Ar\* vs. <sup>40</sup>Ar\* of MORB samples analyzed in this study, all obtained by step crushing (each point represents one crush step). While PR samples consistently show the lowest <sup>4</sup>He/<sup>40</sup>Ar\* ratios and highest <sup>40</sup>Ar\* contents, NPR samples typically have lower <sup>40</sup>Ar\* contents and higher (≥10) <sup>4</sup>He/<sup>40</sup>Ar\* ratios pointing to elemental fractionation during solubilitycontrolled equilibrium between CO2-rich vesicles and basaltic melt, with a potential contribution from fractionation during open-system degassing (for  $^4$ He/ $^{40}$ Ar\* > 40). NPR AL4959-406 is an anomalous NPR sample that, despite its low vesicularity, plots within the range of popping rocks in <sup>4</sup>He/<sup>40</sup>Ar\* vs. <sup>40</sup>Ar\* space. OCC and PRTE-LV samples plot intermediate between PR and NPR samples. Previous data from Péron et al. (2019), as well as the putative mantle production ratio within the range  $3\pm1$  (Jambon et al., 1986; Staudacher et al., 1989; Marty and Zimmermann, 1999), are shown for comparison. Note that we cannot exclude the possibility that the consistently low <sup>4</sup>He/<sup>40</sup>Ar\* of PR samples (horizontal dashed line) actually reflect the mantle production ratio (section 4.1.).

 $^4$ He/ $^{40}$ Ar\*, consistent with estimates for either the mantle production ratio (OCC samples, with  $^4$ He/ $^{40}$ Ar\*  $\sim$ 3.5; Table 1) or degassed MORBs (NPR samples, with  $^4$ He/ $^{40}$ Ar\* up to  $\sim$  40; Tucker et al., 2018) (Fig. 3). Considered altogether, MORB samples analyzed in this study define a general trend where the  $^4$ He/ $^{40}$ Ar\* increases when the concentration of  $^{40}$ Ar decreases (Fig. 3).

## 3.3. Nitrogen and carbon data

Nitrogen and carbon concentrations and isotopic ratios are reported in Table 6. Nitrogen concentrations vary over two orders of magnitude (with PR samples consistently having the highest N contents, up to 3 x 10<sup>-3</sup> cm<sup>3</sup>STP/g). These broadly correlate with <sup>4</sup>He and C concentrations, with C/N ratios varying by two orders of magnitude (from  $\sim 100$  up to > 10,000) (Fig. 4), in line with the range of previously published MORB data (Cartigny et al., 2001; Marty and Zimmermann, 1999). The N isotope composition of MORB samples from 14°N on the MAR exhibit marginal variability (Table 6): average  $\delta^{15}$ N values of PR (-4.4  $\pm$  1.2 %), PRTE-LV (-5.1  $\pm$  1.6 %), NPR (-3.6  $\pm$  1.5 %) and OCC (-4.8  $\pm$  0.8 %) samples are all within error of each other, and in good agreement with the canonical  $\delta^{15}N$  of the upper mantle derived from the analysis of both MORB samples and fibrous diamonds (-5  $\pm$  2 %; Cartigny and Marty, 2013). These values are in good agreement with previous analyses of nitrogen isotopes in popping rocks (e.g., average  $\delta^{15}N$  of -3.5 % for popping rock 2πD43; Javoy and Pineau, 1991). Notably, Labidi et al. (2020) published  $\delta^{15}N$  values for two samples measured here ( $\delta^{15}N =$ -4.8 and -3.2 % for PRTE-LV sample AL4820-43 duplicates, and  $\delta^{15}$ N = -4.0 % for PR sample AL 4821-58), in excellent agreement with data reported in this study ( $\delta^{15}$ N = -3.3 and -5.7 % for AL4820-43 and  $\delta^{15}$ N = -4.2, -5.5 and -3.6 % for AL 4821–58; Table 3). These previous studies had the advantage of being able to assess the extents of potential air contamination for each of the analyzed samples, using 40Ar/36Ar (Javoy and Pineau, 1991) or  $\Delta^{30}$ N (Labidi et al., 2020). This is important, as basalts with low  $^{40}$ Ar/ $^{36}$ Ar have been previously shown to potentially exhibit spuriously low or high  $\delta^{15}N$  relative to their mantle source. In the present study, it is not possible to quantify the extent of nitrogen assimilation during eruption (Marty, 1995; Marty and Humbert, 1997; Marty and Zimmermann, 1999). However, the good agreement between our  $\delta^{15}N$  and previous studies and high  $^{40}Ar/^{36}Ar$ measured on separate aliquots suggests that, although not quantified in the present study, surface nitrogen assimilation is unlikely to be an issue for our samples.

The range of carbon isotope variations across the MORB samples analyzed in this study ( $\delta^{13} C$  from -11.1 to -3.4 %; Table 6) is also comparable to previously published data for MORBs ( $\delta^{13} C$  from -11.4 to -4.3 %; Cartigny et al., 2001), although  $\delta^{13} C$  values as low as -11 % are rather scarce in the literature. The average  $\delta^{13} C$  (-6.7  $\pm$  2.3 %) measured here is indistinguishable from the average MORB value of  $-5.2\pm0.7$  % previously derived by Marty and Zimmermann (1999).  $CO_2/^3 He$  ratios are considered to reflect bulk  $C/^3 He$  (i.e., all the C budget is represented by  $CO_2$ ) (Fig. 5). We find that the average  $C/^3 He$  of PRTE-LV, OCC and NPR samples are  $(2.42\pm0.50)\times10^9$ ,  $(1.81\pm0.79)\times10^9$  and  $(1.95\pm0.43)\times10^9$ , respectively. The average  $C/^3 He$  of PR samples  $((3.33\pm0.52)\times10^9)$  appears slightly higher than the ratios observed for other MORB samples, intermediate between the N-MORB

Table 6
Nitrogen and carbon isotope and elemental data for MORB samples analyzed in this study.

Sample Name	Type	Mass (mg)	N <sub>2</sub> (cm <sup>3</sup> STP/g)	Error (1σ)	δ <sup>15</sup> N (‰)	Error (1σ)	Average	Error (1σ)	mol C/g	δ <sup>13</sup> C
AL4818-003	PR	46.32	1.13x10 <sup>-03</sup>	2.29x10 <sup>-07</sup>	-4.39	0.98	-5.09	0.68	9.50x10 <sup>-06</sup>	-11.13
				re-analysis	-5.74	0.98				
				re-analysis	-5.14	1.01				
L4821-055	PR	101.02	3.01x10 <sup>-03</sup>	5.67x10 <sup>-07</sup>	-2.44	0.96	-2.38	0.49	5.54x10 <sup>-05</sup>	-4.3
				re-analysis	-2.50	0.97				
				re-analysis	-1.68	0.97				
				re-analysis	-3.02	0.97				
				re-analysis	-2.24	0.98				
L4821-058	PR	64.29	1.75x10 <sup>-03</sup>	2.65x10 <sup>-07</sup>	-1.80	1.59	-4.23	2.16	9.33x10 <sup>-05</sup>	-9.0
11-021-030	1 K	04.27	1.75x10	re-analysis	-4.93	1.60	-7.23	2.10	).55X10	- 5.0
				re-analysis	-5.96	1.60				
		62.89	1.60x10 <sup>-03</sup>	2.97x10 <sup>-07</sup>	-4.21	1.59	-5.49	1.19	1.08x10 <sup>-04</sup>	-8.8
				re-analysis	-5.69	1.59				
				re-analysis	-6.58	1.59				
		98.94	2.21x10 <sup>-04</sup>	4.98x10 <sup>-08</sup>	-6.36	1.69	-	-	5.56x10 <sup>-05</sup>	-4.6
			1.97x10 <sup>-03</sup>	2.82x10 <sup>-07</sup>	-2.11	1.58	-3.87	1.14		
				re-analysis	-3.64	1.59				
				re-analysis	-4.66	1.58				
				re-analysis	-2.57	1.59				
			0.40.40404	re-analysis	-4.98	1.59				
AL4821-059	PR	24.85	9.48x10 <sup>-04</sup>	2.09x10 <sup>-07</sup>	− <b>7.</b> 51	1.70	-	-	6.04x10 <sup>-05</sup>	-7.7
AL4820-037	PR	48.82	5.96x10 <sup>-04</sup>	1.22x10 <sup>-07</sup>	-5.89	1.62	-		2.46x10 <sup>-05</sup>	-8.49
AL4818-006	NPR	894.04	3.34x10 <sup>-06</sup>	1.49 x10 <sup>-09</sup>	-4.25	2.25	-	-	1.54x10 <sup>-06</sup>	-6.2
AL4819-029	NPR	275.82	1.11x10 <sup>-05</sup>	4.54x10 <sup>-09</sup>	-3.11	2.59	_	_	1.16x10 <sup>-05</sup>	-8.1
		1518.02	5.45x10 <sup>-06</sup>	1.44x10 <sup>-09</sup>	-3.75	1.13	_	_		
		2003.93	2.70x10 <sup>-05</sup>	7.51x10 <sup>-09</sup>	-3.65	1.02	-3.58	0.58		
				re-analysis	-2.97	0.96				
				re-analysis	-4.43	1.02				
AL4820-032	NPR	980.16	b.d.l.						1.73x10 <sup>-07</sup>	-26.39
AL4820-045	NPR	334.68	2.82x10 <sup>-05</sup>	7.77x10 <sup>-09</sup>	-2.82	1.74	-	-	5.98x10 <sup>-06</sup>	-8.00
AL4824-104	NPR	222.06	9.47x10 <sup>-06</sup>	5.06x10 <sup>-09</sup>	-3.18	2.08	_	_	1.08x10 <sup>-05</sup>	-7.3
		1031.81	1.35x10 <sup>-05</sup>	3.28x10 <sup>-09</sup>	-2.73	1.09	-	-	7.37x10 <sup>-06</sup>	-6.0
AL4959-406	NPR*	1248.96	9.10x10 <sup>-05</sup>	2.16x10 <sup>-08</sup>	-4.68	1.46	-4.62	0.76	3.44x10 <sup>-06</sup>	-3.3
				re-analysis	-5.34	1.44				
				re-analysis	-3.83	1.46				
AL4822-064	OCC	950.17	2.11x10 <sup>-05</sup>	4.86x10 <sup>-09</sup>	-5.01	1.50	-4.51	0.50	2.00x10 <sup>-06</sup>	-4.2
				re-analysis	-4.02	1.50				
				re-analysis	-4.52	1.53				
AL4822-065	occ	603.45	2.02x10 <sup>-05</sup>	5.15x10 <sup>-09</sup>	-5.10	1.74	-	-	3.15x10 <sup>-06</sup>	-6.2
AT 4010 001	DDTE IV	202.2	6.37x10 <sup>-05</sup>	1.58x10 <sup>-08</sup>	4.06	0.02			2 2010-06	7.1
AL4818-001	PRTE-LV	293.3 840.36	0.3/X10	1.30X10	-4.96	0.92	-	-	3.20x10 <sup>-06</sup> 1.21x10 <sup>-05</sup>	-7.13 -4.29
AL4818-002	PRTE-LV	231.95	3.20x10 <sup>-05</sup>	7.69x10 <sup>-09</sup>	-0.50	1.01	_	_	8.45x10 <sup>-06</sup>	-6.3
	<b></b>	903.96	1.57x10 <sup>-04</sup>	3.30x10 <sup>-08</sup>	-4.21	0.83	-4.26	0.14	1.50x10 <sup>-05</sup>	-4.28
		2 30.20		re-analysis	-4.41	0.81	0	•		1.20
				re-analysis	-4.15	0.84				
				=					(continued on	next page
										-

Table 6 (continued)

Sample Name	Туре	Mass (mg)	N <sub>2</sub> (cm <sup>3</sup> STP/g)	Error (1σ)	δ <sup>15</sup> N (‰)	Error (1σ)	Average	Error (1σ)	mol C/g	$\delta^{13}C$
AL4820-040	PRTE-LV	86.29 642.84	5.89x10 <sup>-04</sup>	1.08x10 <sup>-07</sup>	-6.68	0.99	-	-	3.01x10 <sup>-05</sup> 4.20x10 <sup>-05</sup>	-4.54 -3.61
AL4820-041	PRTE-LV	176.24	6.93x10 <sup>-04</sup>	1.21x10 <sup>-07</sup>	-5.63	0.95	-6.14	0.55	2.95x10 <sup>-05</sup>	-4.24
				re-analysis	-5.82	0.97				
				re-analysis	-5.89	0.98				
				re-analysis	-6.99	0.99				
				re-analysis	-6.38	0.97				
		595.88							3.71x10 <sup>-05</sup>	-3.97
AL4820-043	PRTE-LV	149.67	1.51x10 <sup>-03</sup>	2.37x10 <sup>-07</sup>	-1.51	1.58	-3.28	1.56	5.41x10 <sup>-05</sup>	-4.09
112 1020 0 10	1111221	115107	11011110	re-analysis	-3.70	1.58	0.20	1.00	0111110	
				re-analysis	-1.77	1.59				
				re-analysis	-4.81	1.59				
				re-analysis	-4.60	1.59				
		379.70	9.41x10 <sup>-05</sup>	1.75x10 <sup>-08</sup>	-5.68	1.64	-5.68	1.64	6.32x10 <sup>-06</sup>	-11.34
AL4821-049	PRTE-LV	654.93	8.84x10 <sup>-06</sup>	3.10x10 <sup>-09</sup>	-4.80	1.18	_	_	7.18x10 <sup>-07</sup>	-9.02

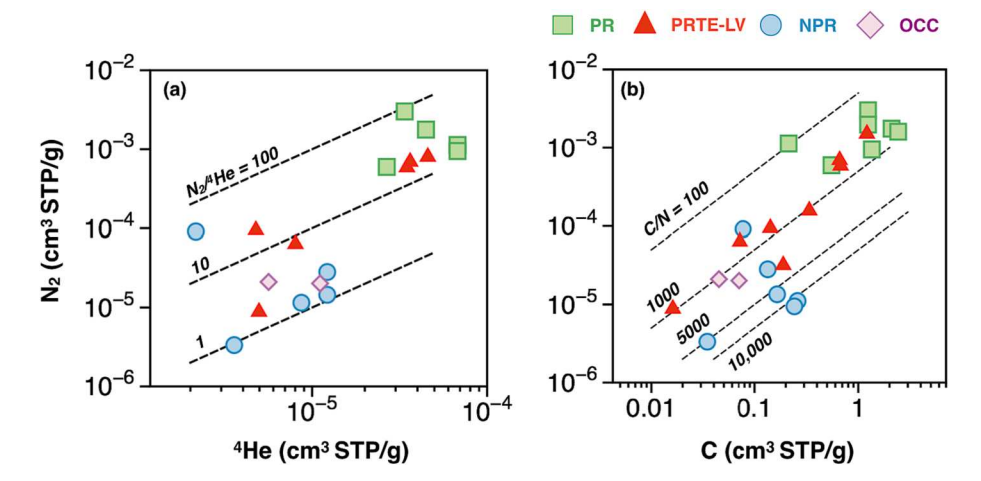
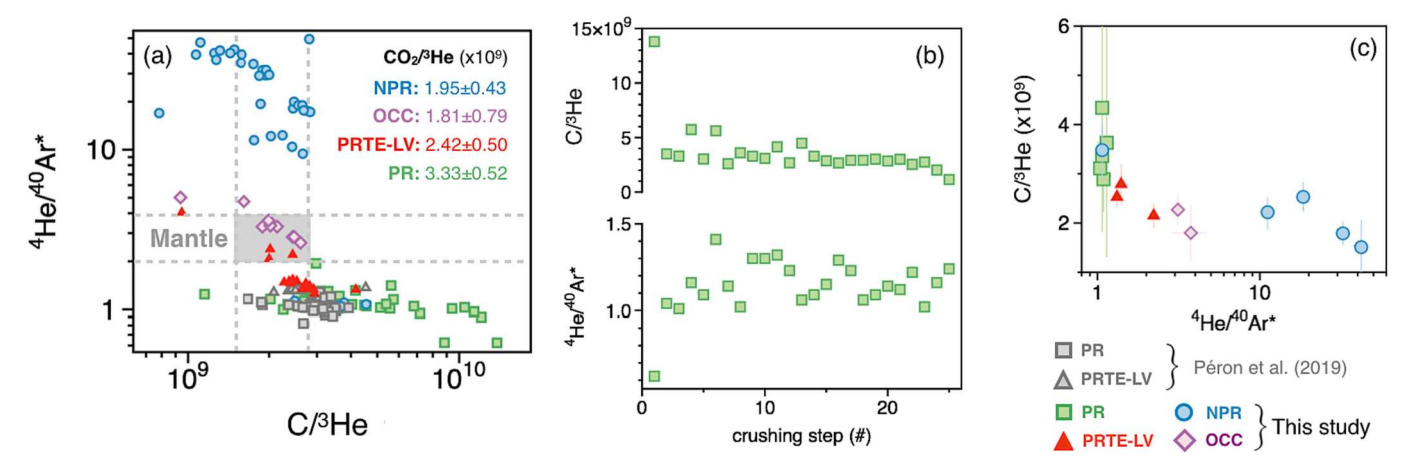


Fig. 4. N<sub>2</sub>-He-C systematics of MORB samples analyzed in this study. (a) N<sub>2</sub>- $^4$ He ratios vary from  $\sim 1$  up to  $\sim 100$ . (b) N<sub>2</sub>-C (whereby C represents CO<sub>2</sub>) systematics also show highly variable C/N ratios from  $\sim 100$  up to  $\geq 10,000$ . In both cases, PR-affiliated samples (i.e., PR and PRTE-LV) generally show higher gas contents than OCC and NPR samples.



**Fig. 5. He-Ar-C systematics of MORB samples analyzed in this study.** (a) Individual step crushing  $^4\text{He}/^{^40}\text{Ar}^*$  vs. C/ $^3\text{He}$  diagram showing that PR samples display a greater average C/ $^3\text{He}$  than other MORB samples. The conventional mantle range (gray area) is shown for comparison. (b) Individual step crushing C/ $^3\text{He}$  and  $^4\text{He}/^{^40}\text{Ar}^*$  as a function of the crushing step number for PR sample AL4821-059. (c) C/ $^3\text{He}$  vs.  $^4\text{He}/^{^40}\text{Ar}^*$  for all MORB samples analyzed in this study (Table 7).

 $((1.4 \pm 0.4) \times 10^9)$  and E-MORB  $((5.9 \pm 1.3) \times 10^9)$  mantle source endmembers previously defined by Marty and Zimmermann (1999).

### 4. Discussion

# 4.1. <sup>4</sup>He/<sup>40</sup>Ar\* systematics and the mantle production ratio

All MORB samples analyzed in this study define a general trend where the  ${}^{4}\text{He}/{}^{40}\text{Ar}^{*}$  becomes higher when the concentration of  ${}^{40}\text{Ar}$ decreases (Fig. 3), as observed in many studies before (e.g., Sarda and Graham, 1990; Sarda and Moreira, 2002; Jones et al., 2019). This feature has been attributed to batch (e.g., Moreira and Sarda, 2000) or Rayleigh-type (Burnard, 1999a) open system degassing, whereby higher <sup>4</sup>He/<sup>40</sup>Ar\* indicate gas loss from the melt. The gas free melt-fraction noble gas fractionated component is thus most visible in samples that have high <sup>4</sup>He/<sup>40</sup>Ar\* and low vesicularities (i.e., OCC and non-popping samples). In this framework, popping rock samples may have mostly preserved their original bulk compositions as a result of minimal gas loss. Assuming the extent of open-system degassing (either via successive batch degassing steps or continuous vesicle nucleation and loss from the magma) has been negligible for these undegassed MORBs would indeed imply that their volatile contents primarily reflect the composition of their mantle sources.

In a closed system, the extent of  ${}^{4}\text{He}/{}^{40}\text{Ar}^{*}$  fractionation is governed by the relative solubilities between He and Ar, which vary by an order of magnitude, such that the maximum fractionation will be about a factor of ten greater than the assumed starting mantle production ratio. For a single episode of batch degassing, closed-system fractionation would thus predict a maximum <sup>4</sup>He/<sup>40</sup>Ar\* ~40, corresponding to the radiogenic production ratio multiplied by the ratio of Ar/He solubilities (i.e.,  $(^{4}\text{He}/^{40}\text{Ar*})_{0} \times \text{K}_{\text{He}}/\text{K}_{\text{Ar}}$ ; with  $\text{K}_{\text{He}} = 6.4 \times 10^{4} \text{ cm}^{3}\text{STP/g}$  and  $\text{K}_{\text{Ar}} = 6.8 \times 10^{4} \text{ cm}^{3}$ 10<sup>5</sup> cm<sup>3</sup>STP/g at 1 bar atm; Jambon et al., 1986; Lux, 1987; Pan et al., 1991; Dixon and Stolper, 1995; Marty, 1995; Jendrzejewski et al., 1997; Hilton et al., 1998; Cartigny et al., 2001; Colin et al., 2013). Importantly, we note that the exact ratio of He and Ar solubilities in basaltic melts depends on the bulk chemical composition (e.g., CO2 and H2O content of the basalt at the time of degassing), as well as the total pressure and temperature (e.g., Yamamoto and Burnard, 2005). Considering plausible ranges of temperature (1000–1500  $^{\circ}\text{C}),$  pressure (0–300 MPa) and volatile contents (0-1.5 wt% for H<sub>2</sub>O and CO<sub>2</sub>), one may expect the K<sub>He</sub>/  $K_{Ar}$  ratio to vary from  $\sim 1$  up to  $\sim 18$ .

The maximum  $^4\text{He}/^{40}\text{Ar}^*$  predicted by closed-system fractionation also strongly depends on the assumed  $^4\text{He}/^{40}\text{Ar}^*$  mantle production ratio (here taken as  $3\pm1$ ; Jambon et al., 1986; Staudacher et al., 1989; Marty and Zimmermann, 1999). For instance, a ( $^4\text{He}/^{40}\text{Ar}^*$ )0 as low as 2 would imply a maximum  $^4\text{He}/^{40}\text{Ar}^*$  ratio  $\sim 20$  for closed-system fractionation (assuming  $K_{\text{He}}/K_{\text{Ar}}=10$ ). In this case, open system conditions involving multiple steps of solubility-controlled fractionation may be required to produce  $^4\text{He}/^{40}\text{Ar}^*$  ratios > 40, i.e., greater than what can be reached under closed-system conditions (e.g., for NPR sample AL4820-045, which exhibits the highest  $^4\text{He}/^{40}\text{Ar}^*$  ( $\sim 42$ ) measured in this study). Hence, while OCC samples do not necessarily require any gas loss, the higher  $^4\text{He}/^{40}\text{Ar}^*$  ( $\geq 10$ ) of NPR samples (Fig. 3) suggests closed-system solubility-controlled equilibrium fractionation and/or fractionation during open-system degassing, depending on the assumed mantle production ratio.

Determining the mantle  $^4\text{He}/^{40}\text{Ar}^*$  production ratio is key to assess the specific mechanisms required to account for the observed  $^4\text{He}/^{40}\text{Ar}^*$  of popping rocks. The range of potential values for the  $^4\text{He}/^{40}\text{Ar}$  production ratio of a given mantle reservoir may vary as a function of time and parent nuclide (U, Th and K) concentrations (e.g., Allègre et al., 1986; Sarda et al., 1985). Here below, we show that, depending on the assumed  $^{232}\text{Th}/^{238}\text{U}$  weight ratio (hereafter noted  $\kappa$ , considered to have varied in the range of 2–4 over the course of Earth's history; Nielsen, 2010) and K/U of the mantle source reservoir, the  $^4\text{He}/^{40}\text{Ar}^*$  production ratio can reach values lower than the canonical  $3 \pm 1$  range,

approaching the value of  $\sim 1$  measured for PR samples. The  $^{4}\text{He}/^{40}\text{Ar}$  production ratio may be calculated either as the ratio of the production rates for radiogenic He and Ar, or as the ratio of accumulated radiogenic He and Ar in a reservoir during a given period of time (in which case radiogenic noble gases measured in MORB vesicles may primarily result from accumulation in the source reservoir). Assuming  $\kappa=4$  and K/U=12,700 (weight ratio as historically determined for a suite of N-MORBs by Jochum et al. (1983) yields a present-day  $^4\text{He}/^{40}\text{Ar}$  production rate (i.e., ratio of  $d^4\text{He}/dt$  to  $d^{40}\text{Ar}/dt$ ) of  $\sim 4.7$  (Fig. 6), markedly higher than measured in PR. Note, however, that this ratio would decrease to  $\sim 3.6$  assuming  $\kappa=2$  (Fig. 6).

Crucially, considering accumulation in the mantle source reservoir over 4 Gyr results in an important lowering of the <sup>4</sup>He/<sup>40</sup>Ar\*. Considering a  $\kappa$  value of 4, the cumulated  ${}^{4}\text{He}/{}^{40}\text{Ar}^{*}$  becomes 1.9 (down to 1.5 if  $\kappa = 2$ ). Most importantly, there is significant uncertainty associated with the K/U of the upper mantle. The Jochum et al. (1983) K/U value of 12,700  $\pm$  400, which has long been considered for estimating the mantle <sup>4</sup>He/<sup>40</sup>Ar\* production ratio is only marginally lower than the most recent estimate of the mean K/U for global MORB (=13,900  $\pm$  200) by Farcy et al. (2020). In 2009, Arevalo et al. (2009) presented a comprehensive examination of MORB samples from the Atlantic, Indian and Pacific oceans and argued for a systematic difference between the K/U of N-MORBs (20,000  $\pm$  2300 (2 $\sigma$ )) and E-MORBs (15,700  $\pm$  3100 (2 $\sigma$ )), respectively. This suggests a bulk depleted MORB mantle K/U of 19,000  $\pm$  2600 (2 $\sigma$ ) (i.e., an upper bound K/U of 21,600), markedly higher than previous estimates from Jochum et al. (1983). Using this value for the K/ U of the popping rock mantle source would allow reproducing the observed <sup>4</sup>He/<sup>40</sup>Ar\* for accumulation times in the range 3 to 4 Gyr (Fig. 6a). Assuming that the K/U of E-MORBs (15,700  $\pm$  3100 (2 $\sigma$ )) is most representative of the mantle source composition of PR, the observed <sup>4</sup>He/<sup>40</sup>Ar\* of PR can only be reproduced by assuming (i) the maximum allowed K/U (=18,800), (ii) the minimum  $\kappa$  value of 2, and (iii) a closed-system accumulation of K and U decay products of  $\sim 4~\text{Gyr}$ (Fig. 6b). Although unlikely, this extreme scenario implies that the possibility for the low <sup>4</sup>He/<sup>40</sup>Ar\* of popping rocks to represent their mantle source composition cannot be discarded.

# 4.2. Implications for popping rock generation

As shown above, we cannot exclude the possibility that the  $^4\text{He}/^{40}\text{Ar}^*$  of popping rocks (1.08  $\pm$  0.04) truly represents the mantle source production ratio, implying that (i) popping rocks have only marginally been affected by secondary processes of gas loss/accumulation, and that (ii) their volatile element inventories can be used as a window into the composition of their mantle source. However, most theoretical predictions of upper mantle source  $^4\text{He}/^{40}\text{Ar}^*$  are greater than the measured popping rock value, unless some extreme parameters (e.g., maximum K/U, minimum  $\kappa$ , and accumulation over the vast majority of Earth's history) are considered (Fig. 6). Thus, the possibility must also be considered that the low  $^4\text{He}/^{40}\text{Ar}^*$  in PR samples results from secondary processes during magma ascent and emplacement at the sea floor.

# 4.2.1. He/Ar fractionation during disequilibrium reactions

Equilibrium degassing should only increase residual  $^4\text{He}/^{40}\text{Ar}^*$  in basaltic melts, therefore a non-equilibrium process, such as preferential diffusive loss of He to  $\text{CO}_2$  bubbles, may be required to explain the  $^4\text{He}/^{40}\text{Ar}^*$  of PR samples that are lower than the mantle production ratio. The idea behind such scenarios of preferential He loss during diffusion-controlled degassing (Gonnermann and Mukhopadhyay, 2007) is that  $\text{CO}_2$  exsolution would produce  $\text{CO}_2$  bubbles with a high He/Ar (due to the preferential diffusion of He), leaving a melt with a low He/Ar ratio. If these vesicles can be lost (i.e., via "open-system degassing"), then the residual melt-vesicle mixture will be left with a lower He/Ar (and lower gas content) than before vesiculation. While this process has been shown to satisfyingly reproduce most MORB data

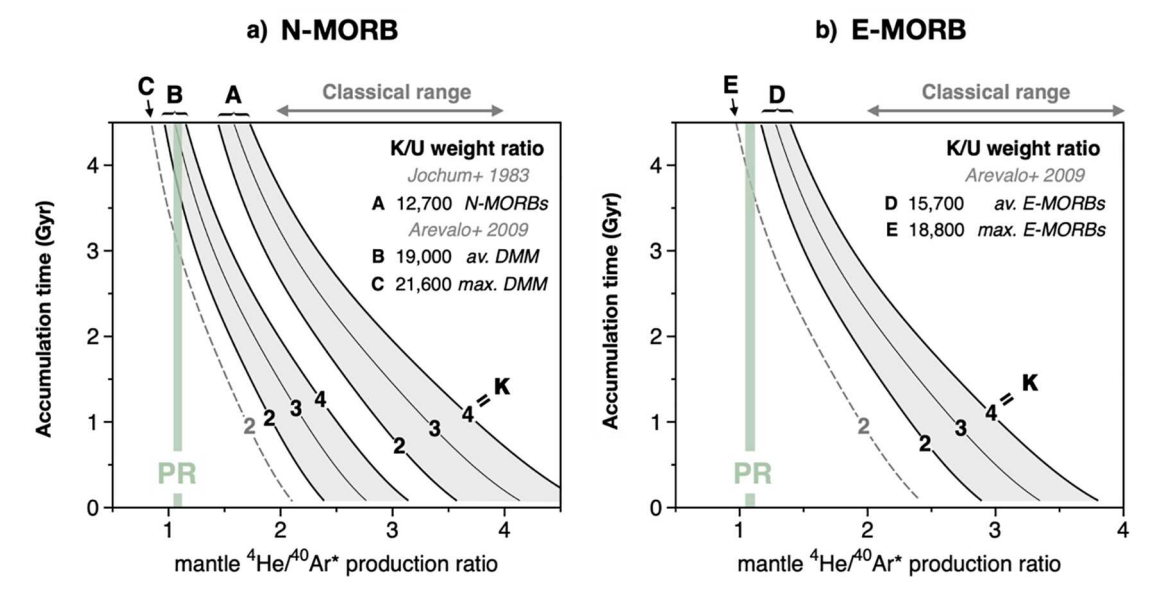


Fig. 6. Theoretical  $^4\text{He}/^{40}\text{Ar}^*$  of the upper mantle source, for typical mantle values of  $\kappa$  (between 2 and 4) and K/U weight ratios from 12,700 (Jochum et al., 1983) up to 21,600 (Arevalo et al., 2009; see legends A-C (a), D-E (b)), as a function of the accumulation time. The accumulation time refers to the duration of radiogenic noble gas accumulation in a closed system prior to the magma emplacement at the sea floor. An accumulation time of zero thus corresponds to the present-day  $^4\text{He}/^{40}\text{Ar}^*$  production rate, while an accumulation time of 3 Gyr would correspond to the  $^4\text{He}/^{40}\text{Ar}^*$  produced by accumulation of U and K decay products over the last 3 Gyr. The classical  $^4\text{He}/^{40}\text{Ar}^*$  mantle production ratio of  $3\pm1$  is shown for comparison using the double arrows at the top of the plots.

(Gonnermann and Mukhopadhyay, 2007), it requires extremely rapid vesiculation in order to avoid re-equilibration, which may only be possible during eruption, where rapid quenching can freeze magma in a disequilibrium state. Such a constraint may not be applicable to popping rocks, which exhibit high vesicularities of up to more than 20 % (Péron et al., 2019; Jones et al., 2019) and vesicle sizes of up to several millimeters (Sarda and Graham, 1990; Jones et al., 2019). Combining the approximate solution (Watson et al., 1982) for vesicle growth timescales with estimates for their *Hadamard-Rybcynski* upwelling velocities relative to the melt (Bottinga and Javoy, 1990) indicates that the time required for generating millimeter-sized vesicles (~150 h) is markedly greater than required for the preservation of disequilibrium (Sarda and Graham, 1990; Watson et al., 1982) (Fig. 7). Under these circumstances,

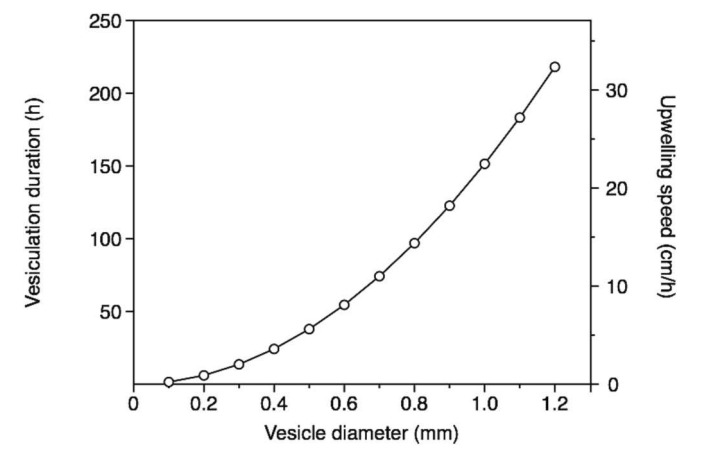


Fig. 7. Simplified model of vesicle growth and upwelling within a basaltic magma. The duration for vesicle growth (t) is computed using the approximate solution of (Watson et al., 1982), where  $t=((r/r_0)^2-1)/(2D(c_i-c_s)/(\rho r_0^2))$ , with r the radius of the bubble,  $r_0$  its initial radius, D the diffusivity of carbonate in the magma  $(1.73 \times 10^{-7}~cm^2/s)$ ,  $c_i$  the initial  $CO_2$  concentration,  $c_s$  the  $CO_2$  concentration at saturation (here, we consider  $c_i-c_s=0.1015~g/cm^3$ ; Sarda and Graham, 1990), and  $\rho$  is the density of the gas  $(1.132~g/cm^3)$ . The upwelling speed relative to the melt is computed as the Hadamard-Rybcynski velocity, following Bottinga and Javoy (1990).

it appears extremely challenging to explain the low <sup>4</sup>He/<sup>40</sup>Ar\* of popping rocks via preferential helium loss during diffusion-controlled degassing (Gonnermann and Mukhopadhyay, 2007).

Another important consideration is that all the  ${}^4\text{He}/{}^{40}\text{Ar}^*$  ratios of PR are measured by crushing, implying that this signature is carried by the vesicles rather than the melt alone. According to the disequilibrium, diffusion-controlled, vesiculation process (Gonnermann and Mukhopadhyay, 2007), the vesicles should have high He/Ar, due to the preferential diffusion of He out of the melt. Accounting for the low <sup>4</sup>He/<sup>40</sup>Ar\* of PR vesicles by this process therefore requires that first generation vesicles have been lost, and that vesicles observed today are in fact of second (or later) generation. In a model where diffusion-driven He/Ar enrichment affects all vesicle generations, the gas phase will invariably exhibit a higher He/Ar than the melt fraction. Producing <sup>4</sup>He/<sup>40</sup>Ar\* lower than the mantle production ratio in vesicles would thus require that the gas free melt-fraction has developed a low enough He/ Ar for the <sup>4</sup>He/<sup>40</sup>Ar\* of subsequent vesicle generations not to be overwhelmed by the preferential diffusion of He (relative to Ar) out of the melt. To have the volatile budget of popping rock vesicles reflecting only a residual fraction of the initial magma content appears incompatible with the extremely high volatile content (and high vesicularities; Table 7) of popping rocks, which makes this unlikely (note that a similar argument is used in section 4.3.2. for C isotope systematics).

## 4.2.2. Evaluating the role of gas accumulation processes

Both the high volatile contents and low <sup>4</sup>He/<sup>40</sup>Ar\* ratios of PR samples could be accounted for by accumulation of "first-generation bubbles" originating from open-system degassing of underlying magmas (Péron et al., 2019). Due to the 10-fold lower solubility of Ar in basaltic melts relative to He (Jambon et al., 1986), bubbles generated at equilibrium from an unvesiculated magma are enriched in Ar relative to He, with <sup>4</sup>He/<sup>40</sup>Ar\* as low as 1/10th the initial (mantle production) ratio. In the case of open system degassing, first-generation bubbles rise towards the surface and may escape from the system (Fig. 8). However, if these bubbles accumulate at depth within a crustal magma reservoir, then a magma with both a high volatile content and low <sup>4</sup>He/<sup>40</sup>Ar\* could be generated, similar to requirements for popping rock generation.

In order to facilitate volatile accumulation, magma storage within a

#### Table 7

Summary of noble gas isotope data for MORB samples analyzed in this study.  $C/^3$ He<sub>4/40</sub> are computed by assuming a  $^4$ He/ $^{40}$ Ar\* mantle production ratio of 3. NPR sample AL4959-406 (noted with an asterisk) is a low vesicularity sample with an average  $^4$ He/ $^{40}$ Ar\* (=1.07) indistinguishable from the range of PR measured in this study (=1.08  $\pm$  0.04). Vesicularity data are from Jones et al. (2019) and Péron et al. (2019). Gas contents are estimated from vesicularity data using previous approach by Javoy & Pineau (1991), assuming the perfect gas law, a rock density of 2.7 g.cm $^{-3}$ , as well as a pressure and temperature of vesicle quenching of 365 bar and 1000 K, respectively.

Sample	Туре	Latitude (deg)	Longitude (deg)	Depth (m)	Vesicularity (%)	Gas content (cm <sup>3</sup> STP/g)	Average <sup>4</sup> He/ <sup>40</sup> Ar*	Error (1σ)	Average $C/^3$ He (x10 <sup>09</sup> )	Error (1σ)	$C/^{3}He_{4/40}$ (x10 <sup>09</sup> )
AL4818-003	PR	13.7737	-45.0108	3672	9–13.6	3.6-5.8	1.07	0.06	3.36	1.41	2.95
AL4821-055	PR	13.7736	-45.0104	3666	17.9-21	8.0-9.8	1.09	0.07	2.89	0.66	2.55
AL4821-058	PR	13.7738	-45.0091	3684	10-11.7	4.1-4.9	1.04	0.05	3.11	0.20	2.72
AL4821-059	PR	13.7710	-45.0090	3706	20.1-24.8	9.3-12.2	1.14	0.15	3.63	2.33	3.23
AL4820-037	PR	13.7675	-45.0081	3773	19.7-20	9.1-9.2	1.07	0.05	4.34	2.52	3.81
AL4818-006	NPR	13.7749	-45.0132	3697	_	_	11.16	1.22	2.22	0.35	3.17
AL4819-029	NPR	13.7755	-45.0499	3566	_	_	32.43	3.62	1.79	0.24	3.18
AL4820-032	NPR	13.7670	-45.0135	3852	_	_	_	-	_	_	_
AL4820-045	NPR	13.7688	-44.9982	3492	_	_	42.01	4.20	1.51	0.55	2.83
AL4824-104	NPR	14.0888	-45.0201	2877	_	_	18.47	0.99	2.53	0.30	4.00
AL4959-406	NPR*	13.8116	-45.0146	3522	_	_	1.07	0.03	3.48	0.57	3.06
AL4822-064	OCC	13.8182	-44.9514	2767	_	_	3.13	0.40	2.27	0.32	2.49
AL4822-065	OCC	13.8179	-44.9513	2749	_	_	3.76	0.91	1.80	0.57	2.05
AL4818-001	PRTE-LV	13.7741	-45.0067	3773	_	_	_	_	_	_	_
AL4818-002	PRTE-LV	13.7743	-45.0074	3761	_	-	2.22	0.16	2.15	0.25	2.20
AL4820-040	PRTE-LV	13.7692	-45.0041	3657	_	_	_	_	_	_	_
AL4820-041	PRTE-LV	13.7695	-45.0026	3645	4.4–6	1.7-2.4	1.32	0.07	2.53	0.21	2.32
replicate	_	13.7695	-45.0026	3645	_	_	_	_	_	_	_
AL4820-043	PRTE-LV	13.7698	-45.0008	3619	_	_	1.40	0.09	2.79	0.41	2.59
AL4821-049	PRTE-LV	13.7796	-45.0120	3821	-	-	-	-	-	-	-

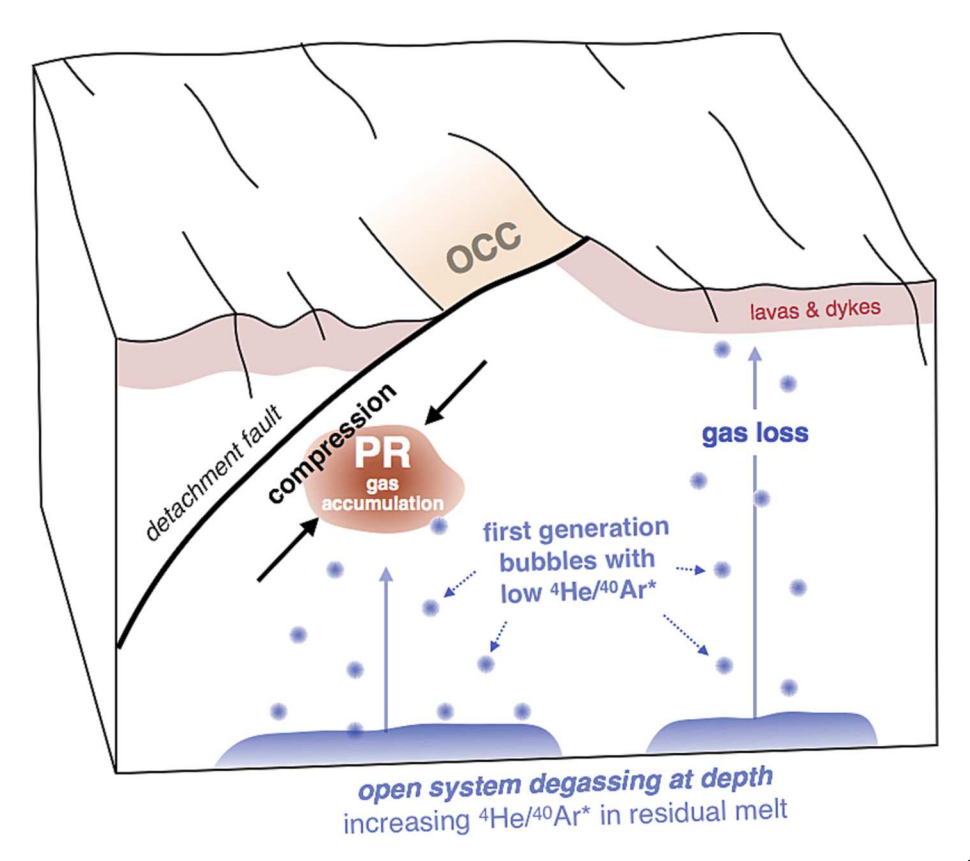


Fig. 8. Simplified representation of the gas accumulation model for generating popping rocks. Both the high volatile contents and low <sup>4</sup>He/<sup>40</sup>Ar\* of PR samples compared to the putative mantle production rate can be accounted for by accumulation of first bubbles generated from open-system degassing of underlying magmas. Bubble accumulation would be promoted by magma storage within a compressional regime associated with bending of the OCC subsurface footwall (e.g., Parnell-Turner et al., 2017), preventing gas loss through the top of the magma reservoir (Jones et al., 2019). This figure is (). adapted from Jones et al., 2019

compressional regime associated with bending of the OCC subsurface footwall (e.g., Parnell-Turner et al., 2017) could prevent gas loss through the top of the magma reservoir. Such a scenario was recently

proposed by (Jones et al., 2019). In this case, the occurrence of popping rocks at the sea floor may primarily require a set of specific tectonic settings allowing for the buildup of a compressional regime and the

protracted accumulation of volatiles (Fig. 8). Considering that compressional regimes associated with the exhumation and formation of oceanic core complexes are ubiquitous in mature, active oceanic detachments (Parnell-Turner et al., 2017) (Fig. 1), we speculate that popping rocks could be rather abundant along the MAR. In fact, they have for instance been found near 36° N on the MAR (Hekinian et al., 1973), where oceanic core complexes have also been reported (Dyment et al., 2018). Another implication of this model is that there should be no reason for popping rocks to only be associated with E-MORBs. If the requirement for specific tectonic settings were to be the main controlling factor for popping rock generation, then popping N-MORBs should occur on the MAR. As such, future expeditions of MORB dredging may demonstrate a compositional variability of popping rocks.

The "first-generation bubble" accumulation model for popping rock generation is not without issues. Vesicle-by-vesicle analyses of popping rocks by Burnard et al. (1997) for instance demonstrated constant CO<sub>2</sub>-<sup>4</sup>He-<sup>40</sup>Ar\* compositions for all the vesicles analyzed (unlike other MORBs), suggesting that Popping rocks are not formed by mixtures of variably degassed magmas. Another important piece of information is that popping rock vesicle size distributions display a decrease of vesicle abundance with vesicle size, often following an exponential law (Sarda and Graham, 1990). This has been shown to also be generally true for the "new" popping rock samples analyzed in this study (Jones et al., 2019). While bubble accumulation processes would likely cause the largest vesicles to be most abundant, the inverse exponential relationship between the size and frequency of vesicles appears most compatible with a continuous process of vesiculation, with only limited vesicle loss (Marsh, 1988; Sarda and Graham, 1990; Burnard, 1999b). Nonetheless, marked increases in the vesicle densities of the largest size classes have been observed for popping rocks with the highest vesicularities (Jones et al., 2019). These deviations from the exponential size-frequency relationship of popping rocks have been interpreted as a direct evidence of vesicle coalescence and/or accumulation processes (Chavrit et al., 2014; Sarda and Graham, 1990; Shea et al., 2010; Jones et al., 2019).

Another point is that, due to their small sizes, the "first-generation bubble" bearing the low He/Ar signature (with  ${}^{4}\text{He}/{}^{40}\text{Ar}^{*} \sim 0.3$ , assuming a mantle <sup>4</sup>He/<sup>40</sup>Ar\* production ratio of 3 and a ratio of He to Ar solubilities  $\sim 10$ ) should have the greatest difficulty to rise through the melt and separate from it (Fig. 7). Significant relative velocities between vesicles and the melt may therefore mostly be achieved for the largest vesicles. In a closed system, the exact <sup>4</sup>He/<sup>40</sup>Ar\* of the gas phase will depend on the relative solubilities of He and Ar, which may greatly vary depending on pressure and temperature conditions (Yamamoto and Burnard, 2005). However, as vesicles appear and grow, noble gases equilibrate and partition into the vesicles such that, for high vesicularities and large vesicle sizes, the <sup>4</sup>He/<sup>40</sup>Ar\* of the bulk gas phase becomes closer to that of the melt prior to vesiculation. Thus, if enough CO2 is available for supersaturation to be maintained until a high vesicularity is reached, the extent of <sup>4</sup>He/<sup>40</sup>Ar\* fractionation should be lower than expected from solubility equilibrium of "first-generation bubbles". These considerations are compatible with the <sup>4</sup>He/<sup>40</sup>Ar\* of popping rocks being only slightly - rather than an order of magnitude - lower than plausible mantle production ratios (Fig. 6).

Taken together,  $^4\text{He}/^{40}\text{Ar}^*$  mantle production ratio estimates, PR vesicle size distribution systematics, and physical considerations for vesicle growth and upwelling through a basaltic magma, indicate that the volatile contents of PR are likely to closely resemble mantle source compositions, with a possibility for samples with the highest vesicularities to have undergone gas accumulation processes (Jones et al., 2019). Here below, we explore the implications for other volatile elements in the upper mantle by considering two scenarios: (A) PR samples have been affected by gas accumulation processes (mantle  $^4\text{He}/^{40}\text{Ar}^*$  production = 3), and (B) PR represent a direct window into the mantle source compositions with no gas accumulation (mantle  $^4\text{He}/^{40}\text{Ar}^*$  production = 1.08  $\pm$  0.04).

### 4.2.3. The special case of NPR sample AL4959-406

NPR sample AL4959-406 exhibits both a PR-like  ${}^{4}\text{He}/{}^{40}\text{Ar}^{*}$  (=1.07; Fig. 3) and a C/ $^3$ He ((3.48  $\pm$  0.57)  $\times$  10 $^9$ ) higher than other NPR samples, but indistinguishable from PR samples. The low  ${}^4\mathrm{He}/{}^{40}\mathrm{Ar}^*$  of NPR AL4959-406 could suggest it has preserved the <sup>4</sup>He/<sup>40</sup>Ar\* of the mantle source, as represented by popping rocks, implying limited (if any) degassing. However, this would be at odds with the common view that low vesicularity samples underwent degassing during magma ascent and emplacement at the seafloor. Reconciling the low <sup>4</sup>He/<sup>40</sup>Ar\* and low vesicularity of NPR AL4959-406 (and most PRTE-LV) may thus require that the mantle source of this sample was relatively carbon-poor, such that barely any CO2 vesicles could have formed over the course of magma evolution. Such a possibility is incompatible with the elevated C/<sup>3</sup>He of this sample relative to other NPR samples. In the framework of the accumulation model, the composition of this sample may require that this sample was exposed to a smaller flux of upwelling bubbles than popping rocks, or that it did not retain as many bubbles as PR. This could potentially be due to a higher magma viscosity for PR relative to NPR AL4959-406, and/or to the spatial variability in the compressional stress field, in line with the NPR AL4959-406 sample being geographically isolated from the rest of the samples analyzed in this study (although from a similar latitude to OCCs; Fig. 1). Another possibility to explain the volatile characteristics of this sample would be preferential He loss (relative to Ar) during magma emplacement (Colin et al., 2013), which could potentially have arisen if the sample for instance had a thinner glass rim than other samples, erupted at shallower depth, and/or cooled

# 4.3. Implications for other volatile elements

# 4.3.1. Correction for solubility-controlled fractionation

<sup>4</sup>He/<sup>40</sup>Ar\* systematics suggest that solubility-controlled fractionation has potentially affected the volatile contents of popping rocks (scenario A). In this case, given the contrasted solubilities of CO<sub>2</sub>, N<sub>2</sub>, and He in basaltic melts, it is clear that solubility-controlled fractionation has the potential to drastically affect C/3He and C/N ratios, potentially leading to misinterpretation of their apparent variations. Accurately determining mantle source ratios thus requires correcting for potential solubility-controlled elemental fractionation during degassing, using the difference between the  ${}^{4}\text{He}/{}^{40}\text{Ar*}$  mantle production ratio and the measured value. Hereafter, C/3He and C/N ratios which are corrected for fractional degassing are denoted as  $C/^{3}He_{4/40}$  and  $C/N_{4/40}$ , respectively. Despite the difference in their vesicularity ( $\sim$ 5 vol% and  $\sim$ 20 vol‰, respectively), PRTE-LV and PR samples exhibit similar <sup>4</sup>He/<sup>40</sup>Ar\* (Fig. 3), potentially lower than the mantle production ratio (see section 4.1.). Only NPR samples (except NPR AL4959-406) clearly exhibit evidence for solubility-controlled fractionation with  $^{4}$ He/ $^{40}$ Ar\*  $\geq$ 10. Most NPR samples also exhibit the highest C/N ratios, suggesting that high C/N values may - at least partially - reflect elemental fractionation during fractional degassing rather than mantle source heterogeneities (Fig. 9). Correction for fractional degassing is therefore carried out following the approach of Marty (1995), assuming a <sup>4</sup>He/<sup>40</sup>Ar\* mantle production ratio of 3 (**scenario A**):

$$C/N_{4/40} = C/N_{measured} \times \left[ \frac{(4He/40Ar)_{measured}}{(4He/40Ar)_{mantle}} \right]^{\left[\frac{K_{-1}^{-1} - K_{-1}^{-1}}{K_{-1}^{-1} - K_{Ar}^{-1}}\right]}$$
(1)

where the K constants represent the solubility coefficients (mol.g<sup>-1</sup>. hPa<sup>-1</sup>) of the corresponding elements. For the sake of simplicity, we consider here  $K_{N_2} = 3.7 \times 10^{-12}$ ,  $K_{CO_2} = 9.0 \times 10^{-12}$ ,  $K_{He} = 2.5 \times 10^{-11}$ , and  $K_{Ar} = 2.6 \times 10^{-12}$ , as previously used by Marty (1995) to correct measured C/N ratios for the effect of fractional degassing. However, and as discussed for He and Ar in section 4.1., the solubility coefficients of N<sub>2</sub> and CO<sub>2</sub> may vary depending on the bulk chemical compositions, as well as the total pressure and temperature (e.g.,

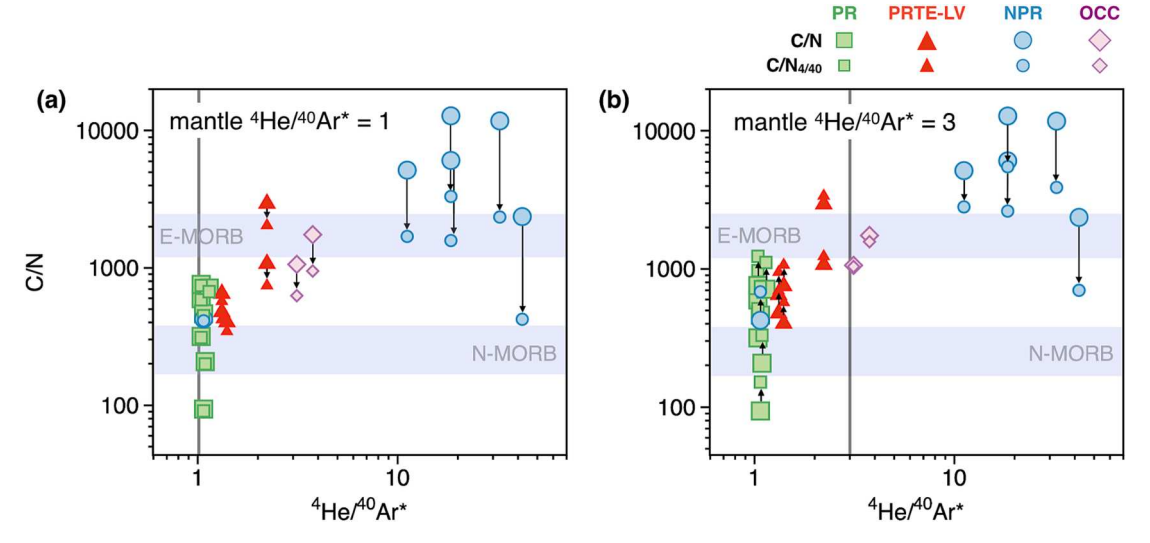


Fig. 9. C/N systematics of MORB samples analyzed in this study, with correction for fractional degassing (black arrows) assuming a mantle  $^4$ He/ $^{40}$ Ar\* production ratio of either 1 (a) or 3 (b). C/N<sub>4/40</sub> values are represented as small symbols at the end of black arrows. E-MORB and N-MORB C/N ranges from Marty et al. (2020) are shown for comparison. This illustrates that E-MORBs (e.g., popping rocks) analyzed in this study exhibit C/N ratios that appear most compatible with the range of C/N ratios previously ascribed to N-MORBs, rather than E-MORBs.

Yamamoto and Burnard, 2005). This is particularly important in the case of vesiculation initiation at great depth (i.e., > 10 km), in which case the question arises as to whether solubilities measured at low pressure are still valid (Sarda and Moreira, 2002). A scenario of deep vesiculation initiation is notably consistent with calculations of  $CO_2$  equilibrium solubility depth for popping rocks with  $\sim 1$  wt%  $CO_2$ , requiring an equilibrium depth of about 30 km (Javoy and Pineau, 1991).

Interestingly, the question of noble gas elemental solubility evolution with pressure was first tackled by theoretical models of liquid state physics (referred to as the "model of hard spheres"; Sarda and Guillot, 2005; Guillot and Sarda, 2006), which demonstrated that vesiculation beginning at depths of  $\sim$  30 km and then followed during ascent by several stages of vesicle loss (when magma slows down or stops) may be able to explain the variability of MORB CO2 and noble gas data. This molecular dynamics approach was then successfully applied to describe the solubility of CO2 (Guillot and Sator, 2011) and noble gases (Guillot and Sator, 2012) in silicate melts of various compositions. This work notably led to the first description of the behavior of a noble gas-bearing CO<sub>2</sub> gas phase in contact with a silicate melt (Aubry et al., 2013), demonstrating that deep-vesiculation, with several stages of vesicle loss during ascent, is indeed able to reproduce the range of noble gas concentrations and elemental ratios observed in the global MORB database, for a large range of vesicularities. In this framework, popping rocks may simply reflect a rare case where little to no vesicle loss has occurred until eruption, possibly because the melt did not slow down sufficiently to decouple from the gas phase on its journey to the surface. Taken together, these considerations suggest we cannot exclude the possibility that vesiculation in ascending melts starts at depths of tens of kilometers, where CO2, nitrogen and noble gas solubilities differ from those measured at ambient pressure, in line with recent experimental work confirming the ability of mafic melts to accommodate remarkably large amounts of CO2 at depth (Amalberti et al., 2021). As a result, solubility coefficients considered for the sake of this exercise should not be taken at face value, and contain important uncertainties. Rather, the following discussion aims at constraining the potential effect of fractional degassing on the C/N (and C/<sup>3</sup>He) systematics of MORBs, for standard solubility coefficient values (Marty, 1995).

As discussed section 4.1. and shown in Eq. (1), the extent of the correction for fractional degassing ultimately depends on the mantle  ${}^4\text{He}/{}^{40}\text{Ar}^*$  production ratio, which remains uncertain. One possibility is that the  ${}^4\text{He}/{}^{40}\text{Ar}^*$  measured for popping rocks represents the mantle

production ratio, in which case no correction for fractional degassing should be done from the measured C/N (and  ${\rm C/^3He}$ ) of popping rocks. Another possibility is that the  ${}^4{\rm He/^{40}Ar^*}$  measured in popping rocks is lower than the actual production ratio of the mantle, which would require the measured C/N (and  ${\rm C/^3He}$ ) to be corrected for solubility-controlled fractionation. Here below, we consider the possible effect of solubility-controlled fractionation on C/N ratios, assuming a mantle production ratio of 3 (Table 8). In this case, we find that the correction for solubility-controlled fractionation would increase the estimated C/N of popping rocks, while decreasing that of NPR samples.

# 4.3.2. Modeling of magmatic degassing

The common absence of a correlation between  $\delta^{15}N$  and  $^4\text{He}/^{40}\text{Ar}^{\star}$ (as observed in this study) has been used to argue against isotope fractionation during degassing being a significant source of N isotope variation in MORBs (Barry and Hilton, 2016). However, the suggestion of a degassing-induced inverse correlation between  $\delta^{13}C$  and  $\delta^{15}N$  within 33 MORB samples from the Southwest Indian Ridge (reported in orange on Fig. 11; Cartigny et al., 2001) was interpreted as reflecting nitrogen isotope fractionation upon degassing, with a direction of the fractionation (favoring the heavy isotopes) opposite to that of carbon isotopes (favoring the light isotopes). While the range of  $\delta^{13}$ C values reported by Cartigny et al. (2001) (-11.40 to -4.36 %) is similar to that observed in this study, these authors observed much larger  $\delta^{15}N$  variations (in the range -5.9 % to +2.1 %) than reported here. These ranges of  $\delta^{13}$ C and δ<sup>15</sup>N variations were interpreted as originating from a common fractionation process (Cartigny et al., 2001). Classical modeling of C and N isotope fractionation during magma degassing usually considers two end-member scenarios referred to as closed (batch degassing, Eq. (2)) and open (Rayleigh distillation, Eq. (3)) system, respectively:

$$\delta X_t = \delta X_0 + 1000 \times \ln(\alpha) \times (X_{melt} - 1)$$
 (2)

$$\delta X_{t} = \delta X_{0} + 1000 \times \ln(\alpha) \times \ln(X_{melt})$$
 (3)

where X refers to the heavy stable isotope of a given element (i.e.,  $^{13}C$  for C,  $^{15}N$  for N),  $\delta X$  refers to the isotopic composition (using delta notation) of this element within the melt, 0 and t refer to before and after degassing, respectively,  $X_{melt}$  is the fraction of this element remaining in the melt at time t, and  $\alpha$  is the equilibrium isotope fractionation factor between the melt and the gas phase for this element (Cartigny et al., 2001). The nitrogen and carbon isotope compositions of the gas and melt

**Table 8** Summary of noble gas isotope data for MORB samples analyzed in this study.  $C/N_{4/40}$  were computed by assuming a  $^4$ He/ $^{40}$ Ar\* mantle production ratio of either 1.04 (lowest ratio determined in this study) or 3 (Jambon et al., 1986; Staudacher et al., 1989; Marty and Zimmermann, 1999).

Sample	Classification	$\delta^{15}$ N (‰)	Error (1σ)	δ <sup>13</sup> C (‰)	C/N (molar)	$C/N_{4/40} = 1$ (molar)	$C/N_{4/40} = 3$ (molar)
AL4818-003	PR	-5.09	0.68	-11.13	94	93	151
AL4821-055	PR	-2.38	0.49	-4.34	207	203	330
AL4821-058	PR	-4.23	2.16	-9.04	596	596	972
	_	-5.49	1.19	-8.89	758	758	1236
	_	-4.05	1.59	-4.65	316	316	515
AL4821-059	PR	-7.51	1.70	-7.73	713	683	1115
AL4820-037	PR	-5.89	1.62	-8.49	462	456	744
	Average:	$-4.95 \pm 1.62$		$-7.75 \pm 2.46$		444 ± 251	$723 \pm 408$
AL4818-006	NPR	-4.25	2.25	-6.22	5175	1729	2821
AL4819-029	NPR	-3.58	0.58	-8.11	11,732	2396	3908
AL4819-032	NPR	-	-	-26.39	-	_	-
AL4820-045	NPR	-2.82	1.74	-8.06	2370	429	700
AL4824-104	NPR	-2.95	2.08	-7.34	12,782	3385	5521
111021101	-	-2.73	1.09	-6.00	6091	1613	2631
AL4959-406	NPR	-4.62	0.76	-3.36	424	418	683
111,505 100	Average:	$-3.49 \pm 0.80$	0.70	$-6.52 \pm 1.78$	,2 ,	1662 ± 1147	2711 ± 1871
11 1000 061	0.00	4.51	0.50	4.00	1000	600	1041
AL4822-064	OCC	-4.51 5.10	0.50	-4.26	1062	638	1041 1577
AL4822-065	OCC	-5.10	1.74	-6.27	1750	967	
	Average:	$-4.81 \pm 0.42$		$-5.27 \pm 1.42$		$803 \pm 232$	1309 ± 379
AL4818-001	PRTE-LV	-4.96	0.92	-7.13	564	_	_
				-4.29	$320^{a}$	_	-
AL4818-002	PRTE-LV	-2.35	1.01	-6.30	2952	2080	3392
	-	-4.26	0.14	-4.28	1074	757	1234
AL4820-040	PRTE-LV	-6.68	0.99	-4.54	573	_	-
				-3.61	699 <sup>a</sup>	_	-
AL4820-041	PRTE-LV	-6.14	0.55	-4.24	477	427	697
				-3.97	649 <sup>a</sup>	581 <sup>a</sup>	948 <sup>a</sup>
AL4820-043	PRTE-LV	-3.28	1.56	-4.09	402	350	572
	-	-5.68	1.64	-11.34	752	656	1069
AL4821-049	PRTE-LV	-4.80	1.18	-9.02	909	_	_
	Average:	$-4.77 \pm 1.45$		$-5.71 \pm 2.50$		809 ± 640	1319 ± 1044

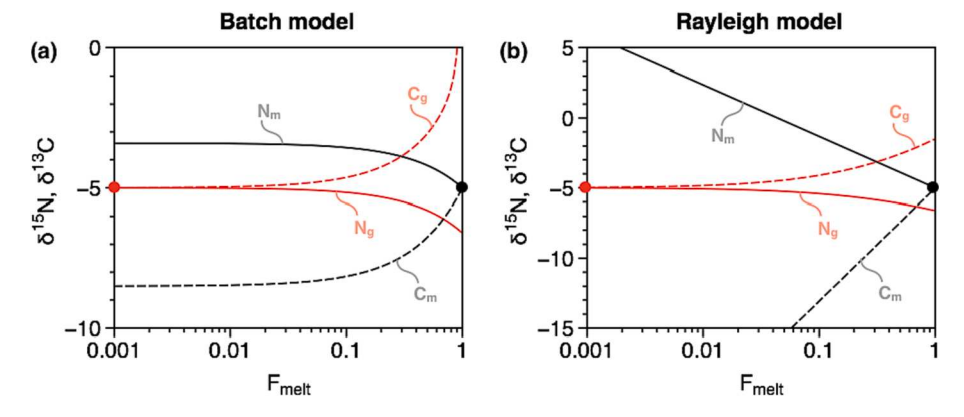


Fig. 10. Nitrogen and carbon isotope compositions as a function of  $F_{melt}$  for batch (a) and rayleigh (b) models, considering equilibrium isotope fractionation factors  $\alpha=0.9984$  and  $\alpha=1.0035$  for nitrogen and carbon, respectively, as derived by Cartigny et al. (2001).  $N_m$  and  $C_m$  refer to the nitrogen and carbon isotope compositions of the melt, respectively.  $N_g$  and  $C_g$  refer to the nitrogen and carbon isotope compositions of the gas, respectively.

are shown as a function of  $X_{melt}$  for both the closed and open system degassing models on Fig. 10, using the equilibrium isotope fractionation factors  $\alpha=0.9984$  and  $\alpha=1.0035$  for nitrogen and carbon, respectively, as derived by Cartigny et al. (2001) from multi-correlations of volatile systematics in Southwest Indian Ridge MORBs. While such modeling remains highly underconstrained, notably because the  $\delta X_0$  and  $\alpha$  values for C and N are both poorly known, these considerations suggest that any of these two models would generate a gas phase that is characterized by higher  $\delta^{13}$ C and lower  $\delta^{15}$ N than the corresponding  $\delta X_0$  (and than the

melt phase). However, our data do not show any evidence for heavy C or light N isotope enrichments relative to the assumed mantle end-member compositions (Fig. 11). Rather, we observe light  $\delta^{13}$ C signatures that would be most consistent with the composition of residual dissolved gas (Fig. 10).

Fractionation upon degassing should produce a linear correlation in a  $\delta^{15}N$  versus  $\delta^{13}C$  diagram, with a slope that will be determined by both the relative solubilities of C and N and their isotope fractionation factors  $\alpha.$  Unfortunately, the ratio of C to N solubilities may greatly vary

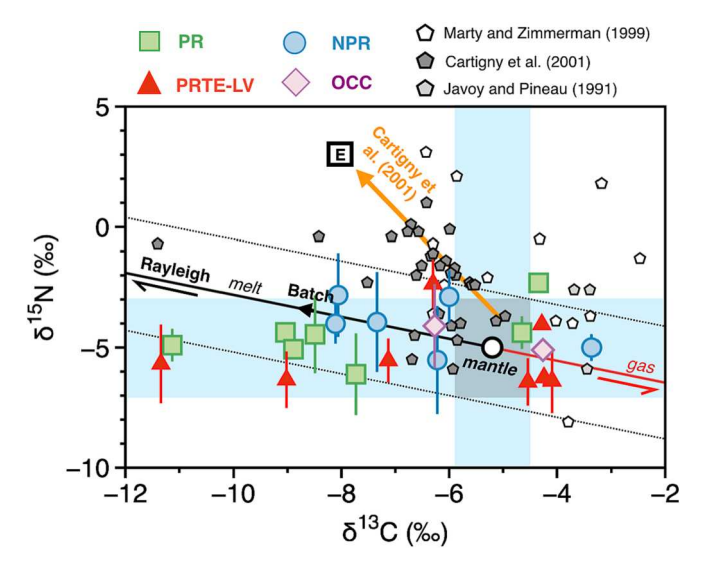


Fig. 11.  $\delta^{15}$ N- $\delta^{13}$ C systematics of MORB samples analyzed in this study and comparison with previously published data. Cartigny et al. (2001) proposed the existence of an inverse correlation between  $\delta^{13}$ C and  $\delta^{15}$ N (orange arrow), suggesting that nitrogen isotopes fractionate upon degassing and that the sign of the fractionation is opposed to that of carbon isotopes. Here, we show the trajectories of the melt (black arrows) and gas phases (red arrow) for nitrogen and carbon isotope fractionation in the framework of the Rayleigh and batch models, starting from a mantle-like composition (white circle, with uncertainties shown as a gray area). The maximum extent of isotope fractionation to be expected for the melt in the framework of the Batch model is shown as a black arrow labeled "Batch". Two samples have  $\delta^{13}C$  as low as -11 ‰, which is markedly more negative than expected for batch degassing, potentially requiring Rayleigh-type fractionation. The surmised composition of the E-MORB end member [E] from Cartigny et al. (2001) is shown for comparison. (For interpretation of the references to colour in this figure legend, the reader is referred to the web version of this article.)

between the initiation of degassing at depth and magma emplacement at the surface (e.g., Yamamoto and Burnard, 2005), therefore making it challenging to make a prediction regarding the expected slope of the  $\delta^{15} N$  -  $\bar{\delta}^{13} C$  correlation line produced by fractionation. For the sake of simplicity, we show on Fig. 11 the expectations for  $\alpha_{N2}=0.9984$ ,  $\alpha_{C}=$ 1.0035, similar solubilities for nitrogen and carbon, and  $\delta X_0$  of -5% for both gases. While the slope of these lines would be much increased if the difference between the carbon and nitrogen solubilities (a factor  $\sim 5$ ) were considered (Cartigny et al., 2001), we note that these simplifying assumptions allow broadly reproducing the observed range of  $\delta^{13}C$ variations, with limited change in  $\delta^{15}N$  (Fig. 11). As such, the observation of variable  $\delta^{13}$ C but homogeneous  $\delta^{15}$ N appears most consistent with the solubility of N not being markedly lower than that of C. For two samples with  $\delta^{13}$ C  $\sim$  -11 % (PR AL4818-003 and PRTE-LV AL4820-043), the  $\delta^{13}$ C appear lighter than expectations for batch fractionation, requiring open system Rayleigh fractionation (Fig. 10, 11). Accounting for the light  $\delta^{13}$ C of PR AL4818-003 with this process however appears inconsistent with any of the two scenarios (A and B) proposed to explain its low  ${}^4\text{He}/{}^{40}\text{Ar}^*.$  Vesicle accumulation (scenario A) would indeed generate heavy C isotope signatures relative to the starting composition, as the gas phase is expected to have a greater  $\delta^{13}C$  than the residual dissolved gas during degassing (Fig. 10). Likewise, to have the <sup>4</sup>He/<sup>40</sup>Ar\* of popping rocks being representative of the mantle production ratio (scenario B) would imply no fractional degassing, and so homogeneous  $\delta^{13}\text{C}$  values across PR samples, which is not observed

More generally, to have the volatile budget of popping rock vesicles reflecting only a residual fraction of the initial magma content appears potentially at odds with the high volatile content (and high vesicularities; Table 7) of these sample. The light  $\delta^{13}$ C of some of the MORB

samples analyzed in this study therefore appear challenging to reconcile with the rest of our observations. One possibility, which appears unlikely but also difficult to firmly rule out, would be that C isotope data suffer from some analytical bias towards light  $\delta^{13}$ C values, possibly as a result of incomplete purification. Such possibility was discarded by introducing Alpha Aesar Copper Oxide(II) and a few grains of crystalline Alpha Aesar Silver Powder (previously baked at 560 °C for at least one hour) within each glass ampoule that was used for CO<sub>2</sub> sampling. Once flame-sealed, samples were baked at 560 °C for another hour in order to quantitatively purify the gas from H<sub>2</sub>O and sulfur-bearing species. Therefore, our favored explanation is that equilibrium isotope fractionation factors a proposed by Cartigny et al. (2001) may not be applicable to MORB samples analyzed in this study. To have the firstgenerated vesicles (potentially accumulated to generate popping rocks, scenario A) exhibiting light C isotope signatures would notably require the  $\alpha_C$  to be < 1. We speculate that the weak  $\delta^{15}$ N-  $\delta^{13}$ C correlation reported and discuss by Cartigny et al. (2001) may actually reflect variable extents of contamination by atmospheric nitrogen, which is difficult to rule out for volatile-poor samples such as Southwest Indian Ridge MORBs, especially when argon isotopes have not been analyzed (Cartigny et al., 2001). Additional work is required to better constrain nitrogen and carbon equilibrium isotope fractionation factors during magma degassing.

### 5. Conclusions

To document the mechanism of popping rock generation and potential effects of degassing and gas accumulation processes on MORB volatile systematics, we have analyzed the volatile element (carbon, nitrogen, noble gas) composition of popping rocks and associated MORBs (n = 19) recently sampled at  $14^{\circ}N$  on the MAR. In line with previous studies, we find that PR exhibit the lowest  $^4\text{He}/^{40}\text{Ar}^{\star}$  (1.08  $\pm$ 0.04) among all MORB samples, lower than the conventional mantle production ratio of 3  $\pm$  1. Such low  ${}^{4}\text{He}/{}^{40}\text{Ar*}$  appear consistent with a formation mechanism involving the accumulation of first-generated bubbles originating from open-system degassing of underlying magmas, implying that the volatile composition of popping rocks does not represent a direct snapshot of un-degassed magmas from the upper mantle. However, several key observations (including vesicle size distributions, and physical considerations for vesicle growth and upwelling through a basaltic magma) argue against this model and rather suggest that the low <sup>4</sup>He/<sup>40</sup>Ar\* of popping rocks correspond to the actual mantle production ratio. Such a possibility cannot be excluded, although it requires an extreme scenario whereby (i) the maximum allowed K/U (=18,800), (ii) the minimum  $\kappa$  value of 2, and (iii) an accumulation time of radiogenic noble gases of  $\sim$  4 Gyr, are considered altogether.

In light of these uncertainties, we explore the implications of degassing processes for volatile element systematics in the upper mantle by considering two scenarios: (A) PR have been affected by gas accumulation processes (i.e., mantle  $^4\mathrm{He/^{40}Ar^*}$  production = 3), and (B) PR represent the mantle source composition (i.e., mantle  $^4\mathrm{He/^{40}Ar^*}$  production = 1.08  $\pm$  0.04). After correction for solubility-controlled degassing fractionation and potential gas accumulation processes using  $^4\mathrm{He/^{40}Ar^*}$  systematics, we find relatively homogeneous C/ $^3\mathrm{He}$  ((2.65  $\pm$  0.51)  $\times$  10 $^9$ ) but variable C/N (from 125 up to 4578). The possible origins of these mantle source geochemical variations at 14°N on the MAR are discussed as part of a companion paper (Part B: mantle source heterogeneities).

The present data set demonstrates the value of combining carbon and nitrogen measurements with major and trace element, vesicularity, as well as noble gas data, along with geological observations provided by the high resolution bathymetry, in order to document the origin and degassing history of volatiles in MORBs. Taken together, the data illustrate the complexities of the mid-ocean ridge systems and the challenges that can be faced when trying to relate MORB analyses to upper mantle source features. In particular, uncertainties associated

with the quantification of the \$^4\text{He}/^{40}\text{Ar\*}\$ mantle production ratio and its potential variability, as well as the potential role of pressure effects on volatile solubilities, remain critical impediments for determining the extent to which the PR volatile compositions are representative of the upper mantle composition. Lastly, we emphasize that PR samples are not N-MORBs, but E-MORBs, implying that their mantle source is geochemically enriched relative to the "normal" upper mantle composition. Interestingly, our data do not show greater C/N for E-MORBs relative to N-MORBs, as yet previously observed for many regions of the globe (Marty & Zimmermann, 1999; Marty et al., 2020). This may be due to the multiplicity of potential sources of geochemical enrichments at mid-ocean ridges (Bekaert et al., Part B), suggesting that deriving a common value for the volatile composition of all E-MORBs worldwide may not be appropriate, and that the volatile element composition of E-MORBs should only be defined on a case-by-case basis.

### Declaration of competing interest

The authors declare that they have no known competing financial interests or personal relationships that could have appeared to influence the work reported in this paper.

### Data availability

Data are available through Zenodo at: https://zenodo.org/records/10033367.

## Acknowledgements

We gratefully acknowledge the Captain, operations teams, marine technicians, and crew of the R/V Atlantis, the operations teams of the AUV Sentry and HOV Alvin, and the entire scientific party on-board AT33-03 and AT40-02 expeditions. We thank Al Gagnon at NOSAMS for assistance with the carbon isotope measurements, as well as Max Jones for constructive discussions. We thank Max Jones for constructive discussions and help with the bathymetric maps used in Fig. 1. We thank Phillipe Sarda, Pierre Cartigny, and two anonymous reviewers for detailed and constructive reviews, as well as Manuel Moreira for careful editorial oversight. Seagoing and analytical efforts were supported by National Science Foundation (NSF) grants OCE-1259218, OCE-1260578, and MGG-2015789 to M. Kurz, E. Mittelstaedt, and P. Barry, respectively.

## Appendix A. Supplementary material

Supplementary material includes an in-depth description of the new analytical protocol for N isotope analysis developed in the Barry Lab at WHOI. This includes three main sections describing the context of these developments, a full description of the analytical methods, as well as a method validation via the analysis of reference material.

Supplementary material to this article can be found online at htt ps://doi.org/10.1016/j.gca.2023.12.015.

# References

- Allègre, C.J., Dupré, B., Lewin, E., 1986. Thorium / uranium ratio of the Earth. Chem. Geol. 56, 219–227.
- Amalberti, J., Sarda, P., Le Losq, C., Sator, N., Hammouda, T., Chamorro-Pérez, E., Guillot, B., Le Floch, S., Neuville, D.R., 2021. Raman spectroscopy to determine CO<sub>2</sub> solubility in mafic silicate melts at high pressure: Haplobasaltic, haploandesitic and approach of basaltic compositions. Chem. Geol. 582.
- Arevalo, R., McDonough, W.F., Luong, M. 2009. The K/U ratio of the silicate Earth: Insights into mantle composition, structure and thermal evolution. Earth and Planetary Science Letters. Elsevier B.V. 278. 361–369.
- Aubry, G.J., Sator, N., Guillot, B. 2013. Vesicularity, bubble formation and noble gas fractionation during MORB degassing. Chemical Geology. Elsevier B.V. 343, 85–98.
- Barry, P.H., Hilton, D.R., 2016. Release of subducted sedimentary nitrogen throughout Earth's mantle. Geochemical Perspectives Letters 2, 148–159.

- Barry, P.H., Hilton, D.R., Halldórsson, S.A., Hahm, D., Marti, K., 2012. High precision nitrogen isotope measurements in oceanic basalts using a static triple collection noble gas mass spectrometer. Geochem. Geophys. Geosyst. 13, 1–16.
- Barry, P.H., Hilton, D.R., Füri, E., Halldórsson, S.A., Grönvold, K., 2014. Carbon isotope and abundance systematics of Icelandic geothermal gases, fluids and subglacial basalts with implications for mantle plume-related CO2 fluxes. Geochim. Cosmochim. Acta 134, 74–99.
- Bonatti, E., Peyve, A., Kepezhinskas, P., Kurentsova, N., Seyler, M., Skolotnev, S., Udintsev, G., 1992. Upper mantle heterogeneity below the Mid-Atlantic Ridge, 0°-15°N. J. Geophys. Res. 97, 4461–4476.
- Bottinga, Y., Javoy, M., 1989. MORB degassing: evolution of CO<sub>2</sub>. Earth Planet. Sci. Lett. 95, 215–225.
- Bottinga, Y., Javoy, M., 1990. MORB degassing: Bubble growth and ascent. Chem. Geol. 81, 255–270.
- Bougault, H., Dmitriev, L., Schilling, J.G., Sobolev, A., Joron, J.L., Needham, H.D., 1988.
  Mantle heterogeneity from trace elements: MAR triple junction near 14°N. Earth Planet. Sci. Lett. 88, 27–36.
- Burnard, P., 1999a. The bubble-by-bubble volatile evolution of two mid-ocean ridge basalts. Earth Planet. Sci. Lett. 174, 199–211.
- Burnard, P., 1999b. Eruption dynamics of "popping rock" from vesicle morphologies. J. Volcanol. Geoth. Res. 92, 247–258.
- Burnard, P., Graham, D., Turner, G., 1997. Vesicle-specific noble gas analyses of popping rock": implications for primordial noble gases in Earth. Science 276 (5312), 568–571.
- Burnard, P., Harrison, D., Turner, G., Nesbitt, R., 2003. Degassing and contamination of noble gases in Mid-Atlantic Ridge basalts. Geochem. Geophys. Geosyst. 4 (1), 1–20.
- Cartigny, P., Pineau, F., Aubaud, C., Javoy, M. 2008. Towards a consistent mantle carbon flux estimate: Insights from volatile systematics (H2O/Ce, δD, CO2/Nb) in the North Atlantic mantle (14° N and 34° N). Earth and Planetary Science Letters. Elsevier B.V. 265, 672–685.
- Cartigny, P., Jendrzejewski, N., Pineau, F., Petit, E., Javoy, M., 2001. Volatile (C, N, Ar) variability in MORB and the respective roles of mantle source heterogeneity and degassing: The case of the Southwest Indian Ridge. Earth Planet. Sci. Lett. 194, 241–257.
- Cartigny, P., Marty, B., 2013. Nitrogen isotopes and mantle geodynamics: The emergence of life and the atmosphere-crust-mantle connection. Elements 9, 359–366.
- Chavrit, D., Humler, E., Grasset, O., 2014. Mapping modern CO<sub>2</sub> fluxes and mantle carbon content all along the mid-ocean ridge system. Earth Planet. Sci. Lett. 387, 229–239.
- Colin, A., Burnard, P., Marty, B., 2013. Mechanisms of magma degassing at mid-oceanic ridges and the local volatile composition (<sup>4</sup>He-<sup>40</sup>Ar\*-CO<sub>2</sub>) of the mantle by laser ablation analysis of individual MORB vesicles. Earth Planet. Sci. Lett. 361, 183–194.
- Dixon, J.E., Stolper, E.M., 1995. An experimental study of water and carbon dioxide solubilities in mid-ocean ridge basaltic liquids. part II: Applications to degassing. J. Petrol. 36, 1633–1646.
- Dosso, L., Hanan, B.B., Bougault, H., Schilling, J.G., Joron, J.L., 1991. SrNdPb geochemical morphology between 10° and 17°N on the Mid-Atlantic Ridge: A new MORB isotope signature. Earth Planet. Sci. Lett. 106, 29–43.
- Dosso, L., Bougault, H., Langmuir, C., Bollinger, C., Bonnier, O., Etoubleau, J., 1999. The age and distribution of mantle heterogeneity along the Mid-Atlantic ridge (31–41°N). Earth Planet. Sci. Lett. 170, 269–286.
- Dyment, J., Szitkar, F., Levaillant, D., 2018. Ridge propagation, oceanic core complexes, and ultramafic-hosted hydrothermalism at Rainbow (MAR  $36^\circ$  N): Insights from a multi-scale magnetic exploration. Earth Planet. Sci. Lett. 502, 23–31.
- Farcy, B., Arevalo Jr, R., McDonough, W.F., 2020. K/U of the MORB Source and Silicate Earth. Journal of Geophysical Research: Solid Earth 125 (12), e2020JB020245.
- Gonnermann, H.M., Mukhopadhyay, S., 2007. Non-equilibrium degassing and a primordial source for helium in ocean-island volcanism. Nature 449, 1037–1040.
- Graham, D.W., 2002. Noble gas isotope geochemistry of mid-ocean ridge and ocean island basalts: Characterization of mantle source reservoirs. Rev. Mineral. Geochem. 47 (1), 247–317.
- Graham, D., Sarda, P., 1991. Reply to comment by T.M. Gerlach on "Mid-ocean ridge popping rocks: implications for degassing at ridge crests". Earth Planet. Sci. Lett. 105, 568–573.
- Graven, H., Keeling, R.F., Rogelj, J., 2020. Changes to Carbon Isotopes in Atmospheric CO2 Over the Industrial Era and Into the Future. Global Biogeochem. Cycles 34, 1–21.
- Guillot, B., Sarda, P., 2006. The effect of compression on noble gas solubility in silicate melts and consequences for degassing at mid-ocean ridges. Geochim. Cosmochim. Acta 70, 1215–1230.
- Guillot, B., Sator, N., 2011. Carbon dioxide in silicate melts: A molecular dynamics simulation study. Geochim. Cosmochim. Acta 75, 1829–1857.
- Guillot, B., Sator, N., 2012. Noble gases in high-pressure silicate liquids: A computer simulation study. Geochim. Cosmochim. Acta 80, 51–69.
- Hekinian, R., Chaigneau, M., Cheminee, J.L., 1973. Popping rocks and lava tubes from the Mid-Atlantic rift valley at 36° N. Nature 245, 371–373.
- Hémond, C., Hofmann, A.W., Vlastélic, I., Nauret, F., 2006. Origin of MORB enrichment and relative trace element compatibilities along the Mid-Atlantic Ridge between 10° and 24°N. Geochem. Geophys. Geosyst. 7 (12).
- Hilton, D.R., McMurty, G.M., Goff, F., 1998. Large variations in vent uid. Nature 396, 359–362.
- Hoernle, K., Hauff, F., Werner, R., Van Den Bogaard, P., Gibbons, A.D., Conrad, S., Müller, R.D., 2011. Origin of Indian Ocean Seamount Province by shallow recycling of continental lithosphere. Nat. Geosci. 4, 883–887.
- Hofmann, A.W., 2007. Sampling Mantle Heterogeneity through Oceanic Basalts: Isotopes and Trace Elements. Treatise on Geochemistry 2, 568.

- Jambon, A., Weber, H., Braun, O., 1986. Solubility of He, Ne, Ar, Kr and Xe in a basalt melt in the range 1250–1600°C. Geochemical implications. Geochim. Cosmochim. Acta 50, 401–408.
- Javoy, M., Pineau, F., 1991. The volatiles record of a "popping" rock from the Mid-Atlantic Ridge at  $14\,^\circ$  N: chemical and isotopic composition of gas trapped in the vesicles. Earth Planet. Sci. Lett. 107, 598–611.
- Javoy, M., Pineau, F., Delorme, H., 1986. Carbon and nitrogen isotopes in the mantle. Chem. Geol.  $57,\,41-62$ .
- Jendrzejewski, N., Trull, T.W., Pineau, F., Javoy, M., 1997. Carbon solubility in Mid-Ocean Ridge Basaltic melt at low pressures (250–1950 bar). Chem. Geol. 138, 81–92.
- Jochum, K.P., Hofmann, A.W., Ito, E., Seufert, H.M., White, W.M., 1983. K, U and Th in mid-ocean ridge basalt glasses and heat production, K/U and K/Rb in the mantle. Nature 306, 431–436.
- Jones, M.P., Wanless, V.D., Soule, S.A., Kurz, M.D., Mittelstaedt, E., Fornari, D.J., Curtice, J., et al., 2019. New constraints on mantle carbon from Mid-Atlantic Ridge popping rocks. Earth Planet. Sci. Lett. 511, 67–75.
- Kurz, M.D., Moreira, M., Curtice, J., Lott, D.E., Mahoney, J.J., Sinton, J.M., 2005. Correlated helium, neon, and melt production on the super-fast spreading East Pacific Rise near 17°S. Earth Planet. Sci. Lett. 232, 125–142.
- Kurz, M.D., Curtice, J., Fornari, D., Geist, D., Moreira, M., 2009. Primitive neon from the center of the Galápagos hotspot. Earth Planet. Sci. Lett. 286, 23–34.
- Labidi, J., Barry, P.H., Bekaert, D.V., Broadley, M.W., Marty, B., Giunta, T., Young, E.D., 2020. Hydrothermal <sup>15</sup>N<sup>15</sup>N abundances constrain the origins of mantle nitrogen. Nature 580, 367–371.
- Le Voyer, M., Cottrell, E., Kelley, K.A., Brounce, M., Hauri, E.H., 2015. The effect of primary versus secondary processes on the volatile content of MORB glasses: An example from the equatorial Mid-Atlantic Ridge (5°N–3°S). J. Geophys. Res. Solid Earth 120. 125–144.
- Le Voyer, M., Kelley, K.A., Cottrell, E., Hauri, E.H., 2017. Heterogeneity in mantle carbon content from CO<sub>2</sub>-undersaturated basalts. Nat. Commun. 8 (1), 14062.
- Lodders, K., 2021. Relative atomic solar system abundances, mass fractions, and atomic masses of the elements and their isotopes, composition of the solar photosphere, and compositions of the major chondritic meteorite groups. Space Sci. Rev. 217, 1–33.
- Long, X., Geldmacher, J., Hoernle, K., Hauff, F., Wartho, J., Garbe-schönberg, D., Grevemeyer, I., 2019. Age and origin of Researcher Ridge and an explanation for the 14°N anomaly on the Mid-Atlantic Ridge by plume-ridge interaction. Lithos 326–327, 540–555.
- Lux, G., 1987. The behavior of noble gases in silicate liquids: Solution, diffusion, bubbles and surface effects, with applications to natural samples. Geochim. Cosmochim. Acta 51, 1549–1560.
- Marsh, B.D., 1988. Crystal size distribution (CSD) in rocks and the kinetics and dynamics of crystallization - I Theory. Contrib. Miner. Petrol. 99, 277–291.
- Marty, B., 1995. Nitrogen content of the mantle inferred from N<sub>2</sub>-Ar correlation in oceanic basalts. Nature 377 (6547), 326-329.
- Marty, B., Almayrac, M., Barry, P.H., Bekaert, D.V., Broadley, M.W., Byrne, D.J., Ballentine, C.J., Caracausi, A., 2020. An evaluation of the C/N ratio of the mantle from natural  $\rm CO_2$ -rich gas analysis: Geochemical and cosmochemical implications. Earth Planet. Sci. Lett. 551, 116574.
- Marty, B., Humbert, F., 1997. Nitrogen and argon isotopes in oceanic basalts. Earth Planet. Sci. Lett. 152, 101–112.
- Marty, B., Sano, Y., France-Lanord, C., 2001. Water-saturated oceanic lavas from the Manus Basin: Volatile behaviour during assimilation-fractional crystallisationdegassing (AFCD). J. Volcanol. Geoth. Res. 108, 1–10.
- Marty, B., Zimmermann, L., 1999. Volatiles (He, C, N, Ar) in mid-ocean ridge basalts: Assessment of shallow-level fractionation and characterization of source composition. Geochim. Cosmochim. Acta 63, 3619–3633.
- Moore, J.G., Batchelder, J.N., Cunningham, C.G., 1977. CO<sub>2</sub>-filled vesicles in mid-ocean basalt. J. Volcanol. Geoth. Res. 2, 309–327.

- Moreira, M., Kunz, J., Allegre, C., 1998. Rare Gas Systematics in Popping Rock: Isotopic and Elemental Compositions in the Upper Mantle. Science 279.
- Moreira, M., Sarda, P., 2000. Noble gas constraints on degassing processes. Earth Planet. Sci. Lett. 176, 375–386.
- Nielsen, S.G., 2010. Potassium and uranium in the upper mantle controlled by Archean oceanic crust recycling. Geology 38, 683–686.
- Pan, V., Holloway, J.R., Hervig, R.L., 1991. The pressure and temperature dependence of carbon dioxide solubility in tholeiitic basalt melts. Geochim. Cosmochim. Acta 55, 1587–1595
- Parai, R., Mukhopadhyay, S., Tucker, J.M., Pető, M.K., 2019. The emerging portrait of an ancient, heterogeneous and continuously evolving mantle plume source. Lithos 346–347. 105153.
- Parnell-Turner, R.E., Mittelstaedt, E., Kurz, M.D., Jones, M.R., Soule, S.A., Klein, F., Wanless, V.D., Fornari, D.J., 2018. The Final Stages of Slip and Volcanism on an Oceanic Detachment Fault at 13°48'N, Mid-Atlantic Ridge. Geochem. Geophys. Geosyst. 19, 3115–3127.
- Parnell-Turner, R., Sohn, R.A., Peirce, C., Reston, T.J., MacLeod, C.J., Searle, R.C., Simāo, N.M., 2017. Oceanic detachment faults generate compression in extension. Geology 45, 923–926.
- Péron, S., et al., 2019. Noble gas systematics in new popping rocks from the Mid-Atlantic Ridge (14°N): Evidence for small-scale upper mantle heterogeneities. Earth Planet. Sci. Lett. 519, 70–82.
- Pineau, F., Javoy, M., Bottinga, Y., 1976. <sup>13</sup>C/<sup>12</sup>C ratios of rocks and inclusions in popping rocks of the mid-atlantic ridge and their bearing on the problem of isotopic composition of deep-seated carbon. Earth Planet. Sci. Lett. 29, 413–421.
- Sarda, P., Graham, D., 1990. Mid-ocean ridge popping rocks: implications for degassing at ridge crests. Earth Planet. Sci. Lett. 97, 268–289.
- Sarda, P., Guillot, B., 2005. Breaking of Henry's law for noble gas and  $CO_2$  solubility in silicate melt under pressure. Nature 436, 95–98.
- Sarda, P., Moreira, M., 2002. Vesiculation and vesicle loss in mid-ocean ridge basalt glasses: He, Ne, Ar elemental fractionation and pressure influence. Geochim. Cosmochim. Acta 66, 1449–1458.
- Sarda, P., Staudacher, T., Allègre, C.J., 1985. <sup>40</sup>Ar/<sup>36</sup>Ar in MORB glasses: constraints on atmosphere and mantle evolution. Earth Planet. Sci. Lett. 72, 357–375.
- Schwartz, D.M., Wanless, V.D., Berg, R., Jones, M., Fornari, D.J., Soule, S.A., Lytle, M.L., Carey, S., 2018. Petrogenesis of alkalic seamounts on the Galápagos Platform. Deep-Sea Research Part II: Topical Studies in Oceanography 150, 170–180.
- Shea, T., Houghton, B.F., Gurioli, L., Cashman, K.V., Hammer, J.E., Hobden, B.J., 2010. Textural studies of vesicles in volcanic rocks: An integrated methodology. J. Volcanol, Geoth, Res. 190, 271–289.
- Smith, D.K., Cann, J.R., Escartín, J., 2006. Widespread active detachment faulting and core complex formation near 13 N on the Mid-Atlantic Ridge. Nature 442 (7101), 440–443.
- Staudacher, T., Sarda, P., Richardson, S.H., Allègre, C.J., Sagna, I., Dmitriev, L.V., 1989.
  Noble gases in basalt glasses from a Mid-Atlantic Ridge topographic high at 14°N: geodynamic consequences. Earth Planet. Sci. Lett. 96, 119–133.
- Stroncik, N.A., Niedermann, S., 2016. Atmospheric contamination of the primary Ne and Ar signal in mid-ocean ridge basalts and its implications for ocean crust formation. Geochim. Cosmochim. Acta 172, 306–321.
- Tucker, J.M., Mukhopadhyay, S., Gonnermann, H.M., 2018. Reconstructing mantle carbon and noble gas contents from degassed mid-ocean ridge basalts. Earth Planet. Sci. Lett. 496, 108–119.
- Ulrich, M., Hémond, C., Nonnotte, P., Jochum, K.P., 2012. OIB/seamount recycling as a possible process for E-MORB genesis. Geochem. Geophys. Geosyst. 13, 1–24.
- Watson, E.B., Sneeringer, M.A., Ross, A., 1982. Diffusion of dissolved carbonate in magmas: experimental results and applications. Earth Planet. Sci. Lett. 61, 346–358.
- Yamamoto, J., Burnard, P.G., 2005. Solubility controlled noble gas fractionation during magmatic degassing: Implications for noble gas compositions of primary melts of OIB and MORB. Geochim. Cosmochim. Acta 69, 727–734.